

1 **Bayesian estimation of past astronomical frequencies, lunar distance, and length of**
2 **day from sediment cycles**

3 **A. Malinverno¹ and S. R. Meyers²**

4 ¹Lamont-Doherty Earth Observatory of Columbia university, Palisades, NY 10964.

5 ²Department of Geoscience, University of Wisconsin–Madison, Madison, WI 53706.

6
7 Corresponding author: Alberto Malinverno (alberto@ldeo.columbia.edu)

8
9 **Key Points:**

- 10 • We present two updated methods for Bayesian astrochronology: TimeOptB and
11 TimeOptBMCMC
- 12 • TimeOptB simultaneously estimates the Earth’s axial precession frequency and the
13 sedimentation rate from cyclostratigraphic data
- 14 • In addition, TimeOptBMCMC simultaneously estimates Solar system *g*-frequencies and
15 *s*-frequencies from cyclostratigraphic data

18 **Abstract**

19 Astronomical cycles recorded in stratigraphic sequences offer a powerful data source to estimate
20 Earth's axial precession frequency k , as well as the frequency of rotation of the planetary
21 perihelia (g_i) and of the ascending nodes of their orbital planes (s_i). Together, these frequencies
22 control the insolation cycles (eccentricity, obliquity and climatic precession) that affect climate
23 and sedimentation, providing a geologic record of ancient Solar system behavior spanning
24 billions of years. Here we introduce two Bayesian methods that harness stratigraphic data to
25 quantitatively estimate ancient astronomical frequencies and their uncertainties. The first method
26 (TimeOptB) calculates the posterior probability density function (PDF) of the axial precession
27 frequency k and of the sedimentation rate u for a given cyclostratigraphic data set, while setting
28 the Solar system frequencies g_i and s_i to fixed values. The second method (TimeOptBMCMC)
29 applies an adaptive Markov chain Monte Carlo algorithm to efficiently sample the posterior PDF
30 of all the parameters that affect astronomical cycles recorded in stratigraphy: five g_i , five s_i , k ,
31 and u . We also include an approach to assess the significance of detecting astronomical cycles in
32 cyclostratigraphic records. The methods provide an extension of current approaches that is
33 computationally efficient and well suited to recover the history of astronomical cycles, Earth-
34 Moon history, and the evolution of the Solar system from geological records. As case studies,
35 data from the Xiamaling Formation (N. China, 1.4 Ga) and ODP Site 1262 (S. Atlantic, 55 Ma)
36 are evaluated, providing updated estimates of astronomical frequencies, Earth-Moon history, and
37 secular resonance terms.

38

39 **Plain Language Summary**

40 Earth's transit through our Solar system is ever evolving, and so are such seemingly unwavering
41 planetary characteristics as the number of hours in a day. For example, it is well known that the
42 length of the day generally increases with time as Earth's rotation rate decreases from tidal
43 interactions with our orbiting moon. But the ability to chart out this evolution over the history of
44 the Solar system has been hampered by limitations of both data and theoretical models. This
45 study presents a computational approach to map out the history of Solar system motions and the
46 history of the Earth-Moon system, including the length of a day, by leveraging geological data
47 and astronomical theory within a statistical framework that fully accounts for uncertainties. As
48 such, the approach provides a means to use the geological archive as an astronomical
49 observatory, allowing us to explore Solar system and Earth-Moon dynamics throughout their
50 long history.

51

52 **1 Introduction**

53 Quasiperiodic variations in Earth's orbit and axis of rotation influence the amount of
54 solar radiation received at the Earth's surface, causing climate variations and corresponding
55 changes in sediment deposition, and resulting in cyclic sediment sequences that provide a
56 geologic archive of the astronomical rhythms. Following the groundbreaking discovery that
57 astronomical cycles, or "Milankovitch cycles" (Milanković, 1941), pace the Pleistocene ice ages
58 (Hays et al., 1976), there has been growing interest in the use of astrochronology to date
59 stratigraphic sequences and constrain the geological time scale, as well as their use to evaluate
60 Earth System and Solar System evolution (Hinnov, 2013; Ma et al., 2017; Meyers, 2019; Meyers

61 & Malinverno, 2018; Olsen et al., 2019; Pälke et al., 2004). This study presents a Bayesian
 62 inversion approach to quantitatively reconstruct ancient astronomical cycles by linking
 63 astronomical theory with geologic observation, building on the framework of Meyers (2015;
 64 M15 hereafter) and Meyers and Malinverno (2018; MM18 hereafter).

65 The periods of the most prominent Milankovitch cycles (eccentricity, obliquity and
 66 climatic precession) are controlled by fundamental Solar system secular frequencies that describe
 67 the frequency of rotation of the planetary orbital perihelia (g_i) and the frequency of rotation of
 68 the ascending nodes of their ecliptic planes (s_i), combined with the precession frequency of the
 69 Earth's spin axis (k). The periods of eccentricity cycles in the Earth's orbit are determined by
 70 differences $g_i - g_j$, while those of the obliquity of the Earth's axis by sums $s_i + k$, and those of
 71 climatic precession (precession modulated by eccentricity) by sums $g_i + k$. We list in Table 1 the
 72 most important cycles used in the present study. The frequencies g_i and s_i are mostly controlled
 73 by the corresponding planet ($i = 1$ for Mercury, 2 for Venus, etc.). The eccentricity and climatic
 74 precession cycles in Table 1 depend on the g_i for the five innermost planets, and the obliquity
 75 frequencies are a function of the s_i for the four innermost planets and Saturn ($i = 6$); s_5 for Jupiter
 76 is zero as a consequence of angular momentum conservation (Fitzpatrick, 2012, p. 180).

77 In principle, ancient sediment records that record Milankovitch cycles can be used to
 78 estimate past variations in climatic precession, obliquity and eccentricity, as well as the
 79 fundamental frequencies (g_i, s_i) and the axial precession frequency (k) from which they derive.
 80 This provides a powerful means to peer into the early history of the Solar System and Earth-
 81 Moon system, analogous to a telescope imaging distant stars and galaxies to reconstruct the
 82 history of the universe (Meyers & Peters, 2022).

83 It has long been known that tidal friction results in a torque that progressively slows
 84 down the Earth rotation and accelerates the Moon, sending it into a higher orbit (e.g., Darwin,
 85 1898). In turn, the slowing of the Earth's spin and increasing lunar distance result in an increase
 86 in the period of the precession of the Earth's axis and a decrease in the axial precession
 87 frequency k . This is a large effect over geologic time scales: models and data indicate that k
 88 decreased from ~ 86 arcsec/yr at 1.4 Ga to a present value of ~ 50.5 arcsec/yr (MM18; Farhat,
 89 Auclair-Desrotour, et al., 2022). In contrast to k , long-term Solar system calculations show that
 90 the fundamental frequencies g_i and s_i did not vary greatly over geologic time (Hoang et al.,
 91 2021). The value of k can therefore be estimated from sedimentary records by comparing
 92 eccentricity frequencies, which do not depend on k , with climatic precession or obliquity
 93 frequencies, which depend on k (see Table 1; MM18; Lantink et al., 2022). Estimates of past
 94 values of k can constrain the past history of the Earth's length of day (LOD) and lunar distance,
 95 informing models for the evolution of tidal dissipation over geological time scales (e.g., Farhat,
 96 Auclair-Desrotour, et al., 2022), and better defining the past values of climatic precession and
 97 obliquity frequencies for astronomical timescale development.

98 Sediment records can also give information on past values of the fundamental Solar
 99 system frequencies g_i and s_i . For example, Olsen et al. (2019) used a long Newark basin Triassic
 100 record (~ 210 Ma) to estimate a period of 1.75 Myr for the $g_4 - g_3$ cycle, compared to its present
 101 period of ~ 2.4 Myr. Zeebe and Lourens (2019) calculated a Solar system solution that best fitted
 102 the Walvis Ridge Site 1262 record, and noted that their solution contains a shift in the $g_4 - g_3$
 103 cycle from a period of ~ 1.5 Myr before 50 Ma to ~ 2.4 Myr (near the present value) afterwards. A
 104 similar shift of the $g_4 - g_3$ cycle was observed by MM18, through the analysis of a segment of
 105 the Walvis Ridge Site 1262 cyclostratigraphic record around 55 Ma. Because of chaotic

106 dynamics, Solar system solutions calculated starting from the present state diverge considerably
 107 at ages beyond ~ 50 Ma (Laskar, 2020), and at earlier ages the period of $g_4 - g_3$ in these model
 108 results fluctuates in a broad range of 1.5-2.6 Myr (Figure 7 of Olsen et al., 2019). Astronomical
 109 cycles recorded in sediments can constrain the value of this long-term periodicity and identify
 110 which computed solutions are consistent with the past Solar system history.

111

112 **Table 1.** Fundamental frequencies of the Solar system (g_i and s_i), axial precession frequency (k), and
 113 astronomical cycle frequencies (eccentricity, obliquity and climatic precession) used in this study and
 114 their present day values. Present day values of g_i and s_i after Hoang et al. (2021); present day value of k
 115 after Farhat, Auclair-Desrotour, et al. (2022).

116

Astronomical frequencies			
	Frequency (arcsec/yr)	Frequency (cycles/kyr)	Period (kyr)
g_1	5.759	0.0044	225.0
g_2	7.448	0.0057	174.0
g_3	17.269	0.0133	75.0
g_4	17.896	0.0138	72.4
g_5	4.257	0.0033	304.4
s_1	-5.652	-0.0044	229.3
s_2	-6.709	-0.0052	193.2
s_3	-18.773	-0.0145	69.0
s_4	-17.707	-0.0137	73.2
s_6	-26.348	-0.0203	49.2
k	50.468	0.0389	25.7
Eccentricity			
	Frequency (arcsec/yr)	Frequency (cycles/kyr)	Period (kyr)
$g_2 - g_5$	3.191	0.0025	406.2
$g_3 - g_2$	9.821	0.0076	132.0
$g_4 - g_2$	10.448	0.0081	124.0
$g_3 - g_5$	13.012	0.0100	99.6
$g_4 - g_5$	13.639	0.0105	95.0
Obliquity			
	Frequency (arcsec/yr)	Frequency (cycles/kyr)	Period (kyr)
$s_6 + k$	24.120	0.0186	53.7
$s_3 + k$	31.695	0.0245	40.9
$s_4 + k$	32.761	0.0253	39.6
$s_2 + k$	43.759	0.0338	29.6
$s_1 + k$	44.816	0.0346	28.9
Climatic precession			
	Frequency (arcsec/yr)	Frequency (cycles/kyr)	Period (kyr)
$g_5 + k$	54.725	0.0422	23.7
$g_1 + k$	56.227	0.0434	23.0
$g_2 + k$	57.916	0.0447	22.4
$g_3 + k$	67.737	0.0523	19.1
$g_4 + k$	68.364	0.0527	19.0

117

118 Astronomical signals recorded by sediment sequences are superimposed on a sizable
119 background of other variability, due to fluctuations in sediment characteristics that are not related
120 to astronomically-driven climatic cycles (e.g., tectonic, geochemical, or ocean circulation
121 changes that influence sedimentation, diagenetic processes). Unrecognized variations in
122 sedimentation rate and hiatuses in sedimentation will also distort the astronomical signals. Many
123 approaches have been developed by the cyclostratigraphic community to recognize astronomical
124 signals, from visual correlation to elaborate quantitative analyses (for an overview, see Sinnesael
125 et al., 2019). The method we present here focuses on 1) simultaneously quantifying uncertainties
126 in the estimated sedimentation rate and astronomical frequencies, and 2) providing a measure of
127 significance of the results to avoid the false detection of astronomical signals in records that do
128 not contain them (Type I errors; Meyers, 2019; Weedon, 2022).

129 In our previous work, M15 established the TimeOpt method, based on how closely
130 stratigraphic data matched Milankovitch periodicities and the expected eccentricity modulation
131 of climatic precession. The method determined a best-fit value for sedimentation rate for
132 prescribed values of five eccentricity frequencies and three climatic precession frequencies
133 (Table 1 of M15). TimeOpt also assessed the statistical significance of the results by comparing
134 the fit obtained for the stratigraphic data to that calculated for random time series of similar
135 statistical characteristics.

136 To extend the methodology and determine from cyclostratigraphic data past values and
137 uncertainties of the astronomical frequencies, MM18 then developed TimeOptMCMC, a Markov
138 chain Monte Carlo method that performs a random walk in the space of the parameters of interest
139 and samples a posterior probability density function (PDF) of sedimentation rate u , of five Solar
140 system frequencies g_i , and of the axial precession frequency k . The posterior PDF combines a
141 prior PDF of the parameters (from information other than that provided by stratigraphic data) and
142 a likelihood function that quantifies how closely data predicted by the parameters fit the
143 stratigraphic data. However, a drawback of TimeOptMCMC is that it typically requires a
144 computationally expensive initial experimentation phase to set up a proposal distribution for the
145 random walk steps that appropriately samples the posterior PDF of the parameters. Once the
146 proposal PDF is properly ‘tuned’, the method is still computationally expensive in its original
147 implementation, typically requiring days to weeks of simulation for each cyclostratigraphic data
148 set.

149 In the present study, we introduce two modified methods that offer significant
150 improvements over the original M15 and MM18 approaches. TimeOptB (‘B’ for Bayesian)
151 extends the TimeOpt methodology of M15 to calculate the posterior PDFs of both sedimentation
152 rate and axial precession frequency, keeping the Solar system fundamental frequencies fixed to
153 characteristic prior values. The statistical significance (‘ p -value’) of the fit of astronomical
154 cycles to the data is also evaluated. TimeOptBMCMC provides a more complete solution by
155 sampling the posterior PDF of sedimentation rate and of all the astronomical parameters of
156 interest: ten Solar system fundamental frequencies (five g_i and five s_i) and the axial precession
157 frequency k . Compared to the previous version, TimeOptBMCMC implements an adaptive
158 sampling strategy that requires no preliminary set up and is orders of magnitude faster in
159 obtaining a useful sample of the posterior PDF. Both methods also account for the possible
160 presence of obliquity cycles (which were not considered in M15 and MM18; however, see
161 Meyers (2019) for TimeOpt applications that include obliquity), implement updated Bayesian

162 priors for the Solar system fundamental frequencies and the axial precession frequency based on
 163 astronomical calculations (Farhat, Auclair-Desrotour, et al., 2022; Hoang et al., 2021), and
 164 include improvements in the approach used for likelihood estimation.

165 The main goal of this paper is to present in detail the TimeOptB and TimeOptBMCMC
 166 methods, applying them to a synthetic data set and to the two data sets previously studied in
 167 MM18 for example demonstrations. The focus of this contribution is on the methodology used to
 168 estimate sedimentation rate and astronomical frequencies, not on the implications of the results
 169 for the history of tidal dissipation and for improvements in astrochronology. Applications of the
 170 methods to the the analysis of a number of records throughout geologic time are currently in
 171 development and will be published in the near future (Ajibade et al., 2023; Wu et al., 2023)

172 In the rest of this paper, we first describe the Bayesian formulation to compute the value
 173 of the posterior PDF for any value of the astronomical parameters of interest. We then explain in
 174 detail the two new methods, compare their results for the two data sets examined by MM18
 175 (Xiamaling Formation, N. China, 1.4 Ga and ODP Site 1262, S. Atlantic, 55 Ma), and describe
 176 how to obtain estimates of lunar distance and length of day and their uncertainties from the
 177 posterior PDF of the axial precession frequency. We conclude by discussing strengths and
 178 limitations of our approach and future improvements.

179 **2 Bayesian Formulation**

180 The vector \mathbf{m} of the parameters of interest consists of the sedimentation rate u , five
 181 values of g_i , five values of s_i , and the precession frequency k as in

$$182 \quad \mathbf{m} = [g_1, g_2, g_3, g_4, g_5, s_1, s_2, s_3, s_4, s_6, k, u]. \quad (1)$$

183 The posterior PDF of \mathbf{m} is defined from Bayes rule as

$$184 \quad p(\mathbf{m}|\mathbf{d}) = \frac{p(\mathbf{m}) p(\mathbf{d}|\mathbf{m})}{p(\mathbf{d})}, \quad (2)$$

185 where the vector \mathbf{d} consists of N sediment property values (e.g., sedimentologic or geochemical
 186 proxy data) measured at constant increments of stratigraphic depth. The two key terms in
 187 Equation (2) are the prior PDF $p(\mathbf{m})$ and the likelihood function $p(\mathbf{d}|\mathbf{m})$. (The denominator $p(\mathbf{d})$
 188 does not depend on \mathbf{m} and is a normalizing constant that is not relevant for the methods
 189 presented here.) The symbols and acronyms used in this paper are listed in Table 2.

190 **2.1 The Prior PDF**

191 The role of the prior PDF is to limit the space of possible parameters to values that agree
 192 with information other than that provided by the stratigraphic data in \mathbf{d} . As there is no
 193 information on prior correlations between the parameters they are taken as independent, so the
 194 prior PDF of \mathbf{m} is simply the product of the prior PDFs of each parameter as in

$$195 \quad p(\mathbf{m}) = p(g_1) p(g_2) \dots p(g_5) p(s_1) \dots p(s_6) p(k) p(u).$$

196 The prior PDF of sedimentation rate u is defined as a uniform distribution between a
 197 minimum and maximum value. These bounds on a realistic value of u can be based on
 198 independent chronostratigraphic information (e.g., radioisotopic dating, bio- or
 199 magnetostratigraphy) or on the environment of deposition (e.g., from the range of sedimentation
 200 rates determined in similar modern and ancient depositional settings).

201 The prior PDFs for the fundamental Solar system frequencies g_i and s_i are the
 202 distributions obtained by Hoang et al. (2021), determined by running a large number of long-
 203 term astronomical solutions starting from slightly different initial conditions. The PDFs of g_i and
 204 s_i are skew Gaussians with some secondary modes, and their parameters are listed in Table 2 of
 205 Hoang et al. (2021) as a function of geologic time. The parameters of the prior PDFs were
 206 obtained from frequencies obtained over intervals of 20 Myr (inner planets, Mercury to Mars) or
 207 50 Myr (outer planets). The prior PDFs of the frequencies g_i and s_i are illustrated in Figure 1 for
 208 ages between the present and 3.3 Ga, a time interval that includes most stratigraphic records
 209 available for astronomical cycle analysis.

210

211

212 **Table 2.** Symbols and acronyms used in this study.

213

Symbols	
a	Semi-major axis of lunar orbit
\mathbf{C}_e	Covariance matrix of residuals \mathbf{e}
\mathbf{d}	Vector of measured sediment property data
\mathbf{d}_{pred}	Vector of data predicted by parameters in \mathbf{m}
\mathbf{e}	Vector of residuals $\mathbf{d} - \mathbf{d}_{\text{pred}}$
g_i	Fundamental Solar system frequencies for the rotation of the planetary perihelia
k	Earth's axial precession frequency
\mathbf{m}	Vector of parameters (g_i, s_i, k, u)
N	Number of data points in vector \mathbf{d}
N_{eff}	Effective number of independent observations in vector \mathbf{d}
N_{sim}	Number of simulated random data sets in significance testing
R^2	Squared correlation coefficient
\mathbf{R}_e	Correlation matrix of residuals \mathbf{e}
r_i	Autocorrelation coefficient of residuals \mathbf{e} at lag i
s_i	Fundamental Solar system frequencies for the rotation of the ascending nodes of the orbital planes
u	Sedimentation rate
σ_e^2	Variance of residuals \mathbf{e}
τ	Lag where the autocorrelation of \mathbf{e} reaches zero
ϕ_i	Coefficient of an AR(P) process
ω	Earth's spin rate
Acronyms	
AR(P)	Autoregressive process of order P
ETP	Eccentricity, tilt, and precession
LOD	Length of day
M15	Meyers (2015)
MM18	Meyers and Malinverno (2018)
MAP	Maximum a posteriori
MCMC	Markov chain Monte Carlo
PDF	Probability density function

214

215

216 The changes in the mean value of the prior PDF and uncertainties of the fundamental
 217 Solar system frequencies in the past are relatively small, a few percent at most. The frequencies

218 associated with the outer planets (g_5 and s_6) vary the least, followed by g_2 . For example, the
 219 Earth eccentricity frequency $g_2 - g_5$ (period ~ 405 ka) has remained nearly constant through
 220 geologic time and has been proposed as a stable anchoring cycle in astrochronology (e.g.,
 221 Hinnov, 2013; Laskar, 2020; Laskar et al., 2004; Olsen et al., 2019).

222 In contrast, the Earth precession frequency k decreased systematically through time due
 223 to tidal energy dissipation. The general trend of k in time can be estimated by modeling tidal
 224 effects and/or by interpolating past geological estimates of k (e.g., Berger & Loutre, 1994;
 225 Laskar et al., 2004). The most recent study is by Farhat, Auclair-Desrotour, et al. (2022), who
 226 calculate past precession frequency from a tidal dissipation model that accounts for changes in
 227 the overall continental distribution and Earth spin rate. The actual history of tidal dissipation,
 228 however, is not accurately known, and estimated past values of k have large uncertainties (e.g.,
 229 Waltham, 2015).

230 We set the prior PDF of k to a normal distribution with a time-dependent mean $\mu_k(t)$ and
 231 standard deviation $\sigma_k(t)$. The prior mean is from a polynomial fit to the past variation of k
 232 calculated by Farhat, Auclair-Desrotour, et al. (2022; see their Figure 6) for ages 0-3.3 Ga, which
 233 is

$$234 \quad \mu_k(t) = 50.4677 + 23.1305 t + 13.0658 t^2 - 11.2346 t^3 + 2.4322 t^4,$$

235 where age t is in Ga. This polynomial accounts for the long-term expected variation of k in the
 236 past, excluding some shorter-term fluctuations at ages < 600 Ma; these shorter-term variations
 237 should be confirmed (or not) by cyclostratigraphic data and not imposed a priori. The tidal
 238 dissipation model of Farhat, Auclair-Desrotour, et al. (2022, p. 4) was deliberately not fitted to
 239 geological data, and it is appropriate to use the trend they computed as the prior mean of k .

240 Farhat, Auclair-Desrotour, et al. (2022) also calculate an uncertainty of the value of k
 241 obtained from their tidal dissipation model, and these uncertainties are small compared to the
 242 uncertainties of k estimated from cyclostratigraphy (see their Figure 6). Our goal is to estimate k
 243 from cyclostratigraphy in a way that is generally consistent with the effects of tidal dissipation,
 244 but the prior standard deviation should be large enough so that the posterior PDF of k we obtain
 245 is not unduly influenced by and provides a test of the tidal modeling results. We therefore set the
 246 prior standard deviation of k using the large uncertainties in the past precession period given in
 247 Waltham (2015), allowing the opportunity for deviations from the Farhat, Auclair-Desrotour, et
 248 al. (2022) tidal model. These uncertainties are a conservative estimate based on substantially
 249 different assumptions about the past history of tidal dissipation, and we assume that they
 250 correspond to \pm two standard deviations. By fitting a polynomial to the fractional uncertainty
 251 (uncertainty divided by the mean) of the precession period given by the JavaScript calculator of
 252 Waltham (2015) between the present and 3.3 Ga, we obtained an expression for the prior
 253 standard deviation of k :

$$254 \quad \sigma_k(t) = (0.0962 t - 0.0262 t^2 + 0.0030 t^3) \mu_k(t).$$

255 The resulting prior PDF of k is shown in Figure 1.

256 **2.2 The Likelihood Function**

257 The likelihood function quantifies how probable it is to observe the measured
 258 stratigraphic data \mathbf{d} when the parameters have the values in \mathbf{m} , and depends on the difference
 259 between \mathbf{d} and a vector \mathbf{d}_{pred} of data predicted by \mathbf{m} . We define an error or residual vector that is

260

$$\mathbf{e} = \mathbf{d} - \mathbf{d}_{\text{pred}}. \quad (3)$$

261

262

263

264

265

266

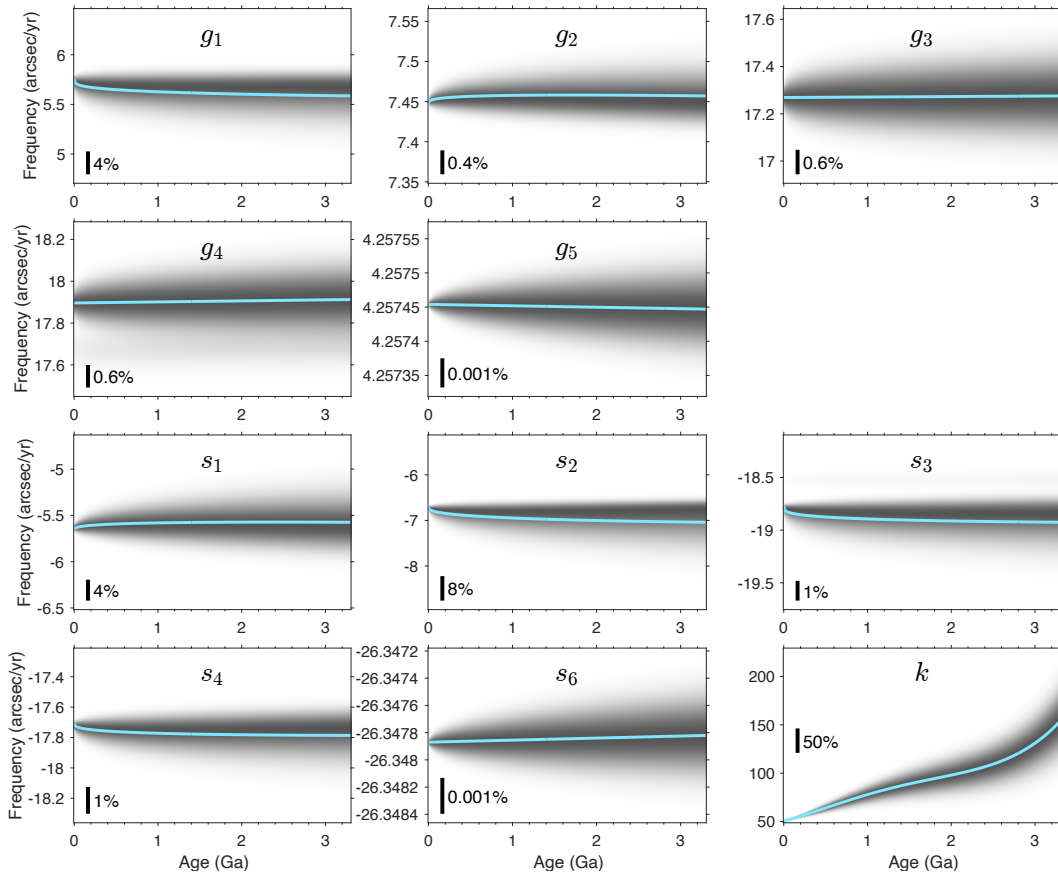
267

268

269

270

271



272

273

274

275

276

277

278

279

280

281

Figure 1. Prior PDFs of astronomical frequencies shown as gray scale images as a function of age (0-3.3 Ga; see the text for details). The blue continuous line shows the prior mean and the black vertical bars display the scale of the overall variations as a percentage of the present value. The Solar system fundamental frequencies g_1 to g_5 , s_1 to s_4 , and s_6 display a much lower variability compared to the systematic decrease with time of the axial precession frequency k .

where \mathbf{R}_e is a symmetric Toeplitz matrix of correlation coefficients with a unit diagonal and constant off-diagonal entries as in

282

$$\mathbf{R}_e = \begin{bmatrix} 1 & r_1 & r_2 & \dots & r_{N-1} \\ r_1 & 1 & r_1 & \ddots & \vdots \\ r_2 & r_1 & 1 & \ddots & r_2 \\ \vdots & \ddots & \ddots & \ddots & r_1 \\ r_{N-1} & \dots & r_2 & r_1 & 1 \end{bmatrix},$$

283

and r_i is the autocorrelation function of \mathbf{e} at lag i ($-1 < r_i < 1$). If the residuals were uncorrelated, \mathbf{R}_e would equal the identity matrix.

284

285

286

287

288

289

290

291

292

293

294

TimeOptB and TimeOptBMCMC use two likelihood functions that measure the fit to two kinds of predicted data. The first (“spectral fit” of M15 and MM18) is based on predicted data \mathbf{d}_{pred} obtained by fitting to the observed stratigraphic data cycles of eccentricity, obliquity, and climatic precession given by the astronomical frequencies and sedimentation rate in \mathbf{m} . The second (“envelope fit” of M15 and MM18) is based on predicting the envelope of a bandpass-filtered climatic precession signal by fitting a combination of cosine and sine functions with the eccentricity frequencies derived from \mathbf{m} . For both the “spectral” and “envelope” evaluation, fitting cosine and sine terms at each astronomical frequency allows estimation of their amplitudes and phases, as in a standard Fourier transform. Details on the calculation of the predicted data in the spectral and envelope fit are in the Supporting Information.

295

296

297

298

299

300

In both the spectral and envelope fit, the residuals in \mathbf{e} are positively correlated. For example, it is well known that stratigraphic data have a “red noise” character and can be modeled as autoregressive processes with positive correlations of nearby values (e.g., Mann & Lees, 1996). It is important to account for these correlations in the likelihood function because they affect the posterior uncertainties of the parameters. Consider a simple case where the parameter of interest is the mean of the observations, estimated from a sample mean μ as in

301

$$\mu = \frac{1}{N} \sum_{i=1}^N d_i.$$

302

303

304

305

306

If the residuals $\mathbf{e} = \mathbf{d} - \mu$ have a variance σ_e^2 and are uncorrelated, the likelihood function of the sample mean would have a variance equal to σ_e^2/N . However, if the residuals are positively correlated there are fewer than N independent observations. For example, if the autocorrelation function of the residuals \mathbf{e} decreased from unity at zero lag to a value near zero at a lag τ , the effective number of independent observations would approximately be

307

$$N_{\text{eff}} \approx N/\tau$$

308

309

310

311

312

313

314

(e.g., Neal, 1993; Priestley, 1981; Zięba, 2010; Zięba & Ramza, 2011). As $N_{\text{eff}} < N$, the sample mean would have a variance $\sigma_e^2/N_{\text{eff}}$ that is greater than in the case where the residuals were uncorrelated. If correlations in the data residuals were ignored, the likelihood function would be artificially concentrated around its mode, causing an underestimation of the uncertainties in the parameters. This could be a substantial bias; in the example of the sample mean, if the data were correlated up to a lag $\tau = 9$, ignoring these correlations would underestimate the posterior uncertainty by a factor of three (measured from the standard deviation).

315

316

317

318

319

Moreover, when the likelihoods for several data fits are combined, it is important to account for differences in the correlations of the residuals. In our application, the residuals in the spectral fit are clearly less correlated than the much smoother residuals in the envelope fit. Ignoring this difference in the correlations would not properly weigh the importance of each data fit in constraining the parameters.

320 An outstanding problem in defining the likelihood function in Bayesian inference is that
 321 the variance and autocorrelation of the residuals \mathbf{e} are typically unknown and cannot be
 322 confidently set a priori. On the other hand, the data may be informative about the statistical
 323 properties of the residuals. For example, fitting a few harmonic components as in the spectral fit
 324 will always result in non-zero residuals, and the statistics of these residuals may be used to infer
 325 the residual variance and autocorrelation.

326 One way to extract this information is to follow a hierarchical Bayes strategy (Gelman et
 327 al., 2004; Malinverno & Briggs, 2004) by adding σ_e^2 and parameters that define the correlation
 328 matrix \mathbf{R}_e to the unknowns of the problem as “hyperparameters.” The original TimeOptMCMC
 329 of MM18 implemented this strategy by adding to the parameter vector two hyperparameters for
 330 each of the spectral and envelope fit: the variance of the data residuals σ_e^2 and the coefficient ϕ_1
 331 of an autoregressive process of order 1 that defined their autocorrelation. These four
 332 hyperparameters were then sampled by MCMC, and the sampled values were used to define the
 333 covariance matrix \mathbf{C}_e when calculating the likelihood at each iteration. The final histogram of the
 334 sampled σ_e^2 and ϕ_1 described their posterior PDFs (Fig. S4, S7, and S10 of MM18).

335 In the updated methodology presented here, we apply an empirical Bayes strategy, where
 336 values of the hyperparameters are estimated from the data, e.g., by choosing their maximum
 337 likelihood value (Carlin & Louis, 2000; Casella, 1985). While hierarchical Bayes fully accounts
 338 for the posterior uncertainty of the hyperparameters, empirical Bayes simplifies the calculations,
 339 speeds up the inversion, and can return a posterior PDF for the parameters in \mathbf{m} that is close to
 340 that obtained by hierarchical Bayes (see the discussion of Figure 9 in Malinverno & Briggs,
 341 2004).

342 The rest of this section describes the form of the likelihood function for the spectral and
 343 envelope fits. Assuming that there are no correlations between the residuals obtained in the two
 344 fits, the total likelihood is simply the product of the spectral and envelope likelihoods.

345 **2.2.1 Likelihood for the Spectral Fit**

346 The spectral fit likelihood is based on modeling the residuals \mathbf{e} in Equation 3 as an
 347 autoregressive process of order 2, or AR(2), as in

$$348 \quad e_i = \phi_1 e_{i-1} + \phi_2 e_{i-2} + w_i, \quad (4)$$

349 where the vector \mathbf{w} is white noise, a sequence of uncorrelated normally distributed values that
 350 have zero mean and a variance σ_w^2 . The AR process exploits the correlations in the vector \mathbf{e} to
 351 predict the i -th value e_i with a linear combination of nearby values, while the driving noise term
 352 w_i accounts for unpredictable random effects. If the time series in \mathbf{e} is adequately modeled by an
 353 AR(2) process, the resulting \mathbf{w} (which can be obtained by solving Equation 4 for w_i) should be
 354 white noise. This can be verified by computing the sample autocorrelation of the estimated \mathbf{w} and
 355 checking that the autocorrelation values are not significantly different from zero for nonzero
 356 lags. Whereas cyclostratigraphic analyses often assume that stratigraphic records can be modeled
 357 as an AR(1) process (e.g., MM18; Mann & Lees, 1996), we found that in several cases an AR(2)
 358 process is necessary to produce a vector \mathbf{w} that is close to white noise. A general description of
 359 AR processes can be found in treatments of time series analysis (Chatfield, 1989; Cox & Miller,
 360 1965; Priestley, 1981).

361 Dettmer et al. (2012) proposed a way to simplify the evaluation of a multivariate normal
 362 likelihood if the residuals \mathbf{e} can be modeled as an AR process. In the AR(2) process (Equation 4),
 363 values e_i can be predicted by e_{i-1} and e_{i-2} plus a driving noise w_i that is uncorrelated. Therefore,
 364 the residuals \mathbf{e} contain a predictable component and a random component \mathbf{w} ; if we subtract the
 365 predictable component of \mathbf{e} , the likelihood function can then be written as the PDF of the
 366 uncorrelated driving noise \mathbf{w} . This simplifies considerably the calculation of the likelihood
 367 because the covariance matrix of \mathbf{w} is diagonal. To complete the calculation of the spectral fit
 368 likelihood, we apply an empirical Bayes strategy and estimate the AR(2) coefficients ϕ_1 and ϕ_2
 369 and the variance σ_w^2 of the driving noise \mathbf{w} from the residuals \mathbf{e} (Andersen, 1974; Burg, 1967;
 370 Ulrych & Bishop, 1975). Details on the estimation of ϕ_1 , ϕ_2 , and σ_w^2 and on the equation for the
 371 spectral fit likelihood are in the Supporting Information.

372 **2.2.2 Likelihood for the Envelope Fit**

373 It seems reasonable to apply the same methodology to the evaluation of the likelihood of
 374 the envelope fit. However, an AR(P) model is not a good representation of the residuals of the
 375 envelope fit, even if the order P is high. The reason is that these residuals \mathbf{e} are the difference of
 376 two low-frequency band-limited signals: the envelope of a filtered climatic precession signal in
 377 the data (\mathbf{d} in Equation 3) minus the sum of harmonic components with the periods of
 378 eccentricity (\mathbf{d}_{pred}). Therefore, the residuals in the envelope fit are very smooth and cannot be
 379 well reproduced by an autoregressive process driven by uncorrelated noise.

380 The likelihood of the envelope fit instead uses an effective number of independent
 381 observations $N_{\text{eff}} = N/\tau < N$, based on an estimate of the lag τ where the autocorrelation of the
 382 envelope fit residuals reaches zero (Zięba, 2010; Zięba & Ramza, 2011). Details on the bandpass
 383 filtering to extract the climatic precession signal in the data (Zeeden et al., 2018), on the
 384 calculation of the predicted precession envelope, on the estimation of the lag τ , and on the
 385 equation for the envelope fit likelihood are in the Supporting Information.

386 **3 TimeOptB Methodology**

387 As the Solar system frequencies g_i and s_i do not vary greatly throughout geologic time
 388 (Figure 1), in TimeOptB we fix these frequencies to their prior mean value at the time of
 389 sediment deposition, so that the only variable parameters in \mathbf{m} are the sedimentation rate u and
 390 the axial precession frequency k . The value of the likelihood, prior PDF, and posterior PDF can
 391 then be calculated over a 2-D grid of u and k . The boundaries of this grid can be initially set to
 392 span the range of the prior PDF and can then be narrowed to resolve details of the posterior PDF.

393 Compared to the original TimeOpt of M15, the major enhancements in TimeOptB are
 394 that 1) the axial precession frequency k is not fixed but is a variable that is estimated from the
 395 data and 2) that the Bayesian formulation provides a measure of uncertainty in the values of u
 396 and k consistent with the data.

397 The significance of astronomical cycles inferred from noisy stratigraphic data is an
 398 outstanding issue, and it has been claimed that false detection of such cycles is likely widespread
 399 in existing studies (Smith, 2023; Weedon, 2022). As done in TimeOpt, we implemented in
 400 TimeOptB a simple Monte Carlo procedure to investigate the statistical significance of the
 401 detected astronomical cycles. The procedure is based on generating a large sample of N_{sim}
 402 random simulated data series that are AR(2) processes with coefficients ϕ_1 and ϕ_2 equal to those

403 estimated from the observed data for the maximum a posteriori value (MAP) values of u and k .
 404 In each of these N_{sim} data sets, we repeat the TimeOptB procedure for the spectral fit over the
 405 range of u and k explored with the measured data and retain the maximum value of the Pearson
 406 R^2 correlation coefficient (the ratio of the variances of the data predicted by fitting astronomical
 407 cycles over the total variance). We then compare the maximum spectral fit R^2 values obtained in
 408 each of the N_{sim} simulated data sets to the R^2 obtained for the actual data at the MAP values of u
 409 and k . (It should be noted that in each of the simulated data series the maximum R^2 will be
 410 obtained for values of u and k that are different than the MAP values in the measured data.)

411 Following the general philosophy of significance testing (Hacking, 2001) we define a p -
 412 value as the fraction of N_{sim} cases where the R^2 of the simulated data sets is as large or larger
 413 than the R^2 in the measured data. If the data contain significant astronomical cycles, a
 414 comparable fit should only occur rarely in the random simulated data sets and the p -value should
 415 be small. To further investigate astronomical cycle significance, we also repeat the same Monte
 416 Carlo procedure separately for cycles of eccentricity, obliquity, and climatic precession. Whereas
 417 the critical significance test is for all the astronomical cycles, the results of the Monte Carlo
 418 experiment when only one set of cycles is considered will highlight which cycles are most
 419 informative in a particular cyclostratigraphic data set.

420 The accuracy of the p -value estimated in this Monte Carlo procedure will obviously
 421 improve as N_{sim} grows; we suggest $N_{\text{sim}} \geq 1,000$. Even if N_{sim} is large, the estimated p -value is
 422 not assured to be the same in different runs of N_{sim} Monte Carlo simulations. In practice, it may
 423 be the case that no simulated data set reaches the fit level observed for the measured data; in that
 424 case, all that can be concluded from the Monte Carlo experiment is that the p -value is $< 1/N_{\text{sim}}$.

425 **4 TimeOptB example results**

426 **4.1 ETP curve (45 Ma)**

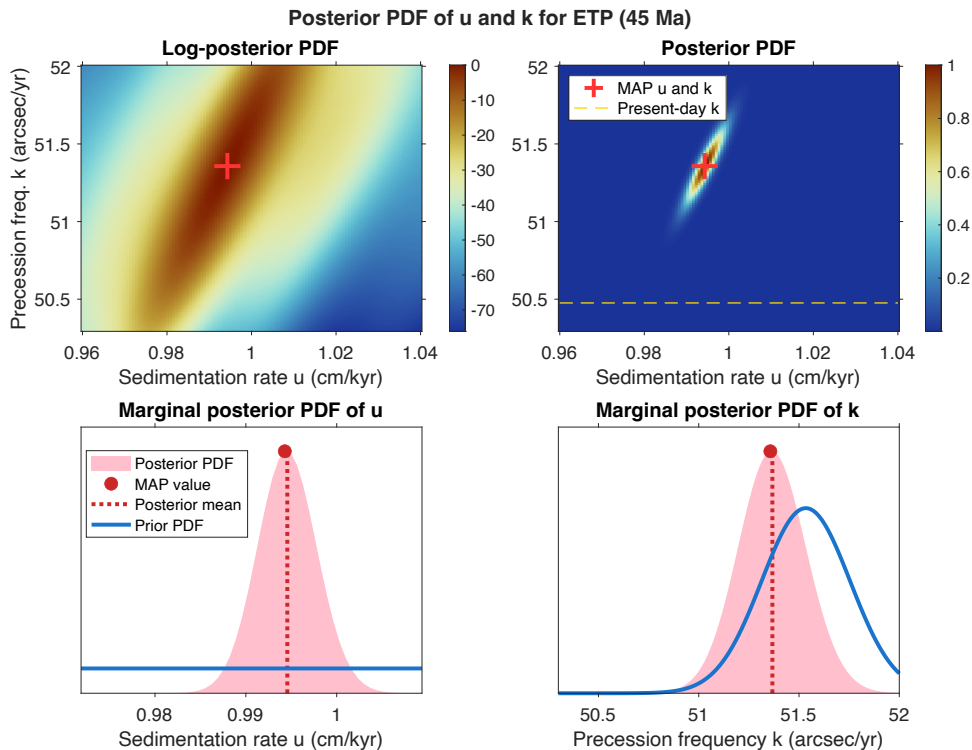
427 To evaluate the efficacy of the TimeOptB approach, we test it against a synthetic data set
 428 that consists of known astronomical signals plus random noise. An ETP astronomical signal is
 429 constructed as the sum of eccentricity, obliquity (tilt), and climatic precession from the solution
 430 of Laskar et al. (2004). The synthetic record consists of 1000 data points spanning a 1 Myr
 431 interval centered on an age of 45 Ma and was converted to depth assuming a sedimentation rate
 432 of 1 cm/kyr. Each of the three astronomical signals was normalized to zero mean and unit
 433 variance before their summation. A time series of AR(1) correlated noise ($\phi_1 = 0.8$) was added to
 434 the astronomical signals to obtain the final synthetic data set. The noise variance was adjusted so
 435 that the variance of the astronomical signals was 0.44 times the total variance (a value of $R^2 =$
 436 0.44 is close to that obtained for the stratigraphic data sets that will be shown later).

437 Images of the log-posterior and posterior PDFs as a function of sedimentation rate u and
 438 axial precession frequency k are shown in Figure 2. The posterior PDF images display a strong
 439 positive correlation between u and k , which is intrinsic to the estimation of astronomical periods
 440 from stratigraphic data. If the stratigraphic data contain a cycle with a distinct spatial wavelength
 441 attributed to an astronomical cycle, the temporal frequency of that cycle will be a function of the
 442 sedimentation rate; if the sedimentation rate were higher, the frequency of the astronomical cycle
 443 will increase correspondingly (see also the discussion).

444 The marginal posterior PDFs of u and k in Figure 2 are obtained by integrating the
 445 images in the vertical and horizontal directions, respectively. The posterior means of u and k

446 (0.995 cm/kyr and 51.367 arcsec/yr) are very close to the sedimentation rate used in the synthetic
 447 example and to the axial precession frequency at 45 Ma in the Laskar et al. (2004) calculations
 448 (which is 51.707 arcsec/yr, from their Equation 40). Notably, if the sedimentation rate were
 449 increased by 0.5% to the exact value of 1 cm/yr, the posterior mean axial precession would
 450 increase by the same amount to 51.624 arcsec/yr, getting even closer to the value expected in the
 451 ETP signal.

452 The fit to the data and to the precession envelope for the maximum a posteriori (MAP)
 453 value of u and k is shown in Figure 3. The R^2 for the data fit is 0.61, which is greater than the
 454 0.44 value used to construct the synthetic data set. This is due to a small amount of variance in
 455 the added noise being attributed to astronomical cycles. The periodogram of the ETP data
 456 (Figure 3c) shows a close correspondence with the spectral lines of the astronomical cycles.
 457

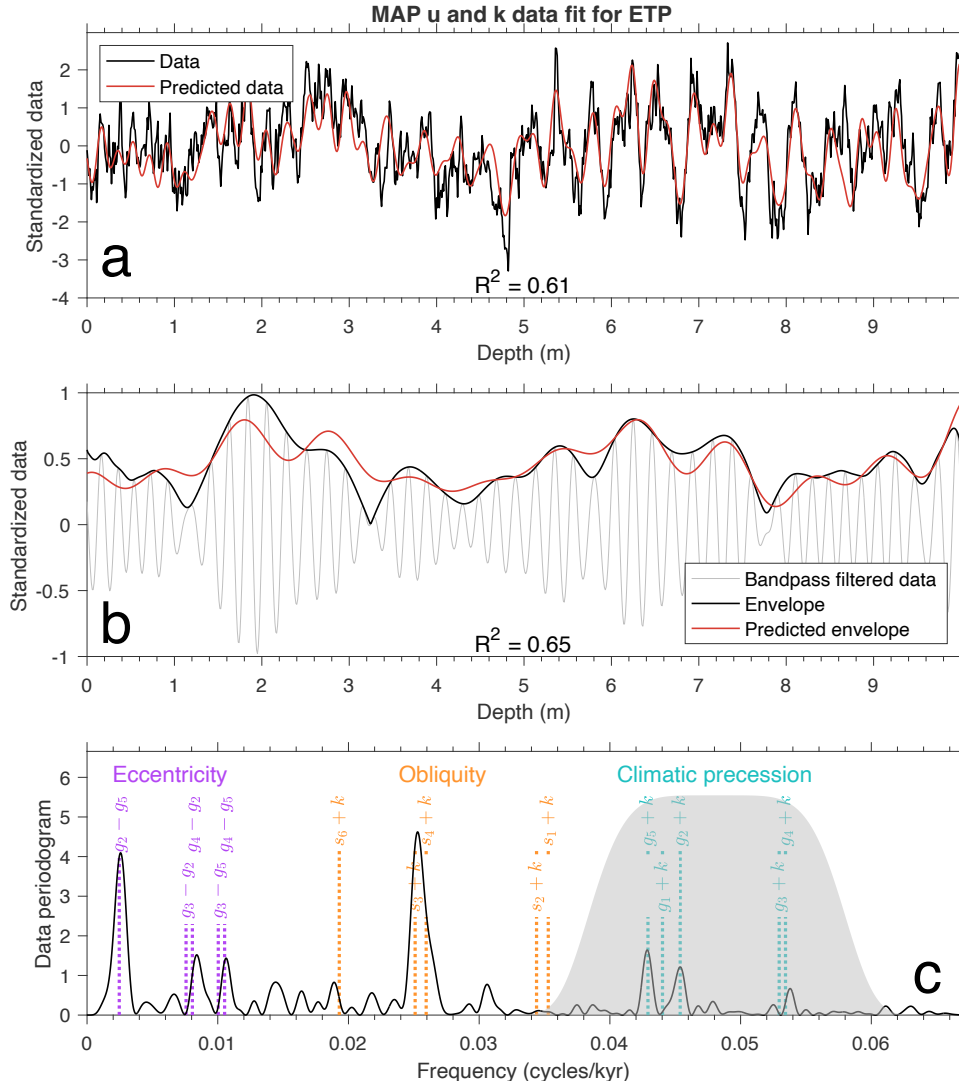


458
 459
 460 **Figure 2.** Posterior PDFs of sedimentation rate u and axial precession frequency k obtained by TimeOptB
 461 from the synthetic ETP test data set. In the PDF images, the log-posterior PDF is normalized to a MAP
 462 value of zero and the posterior PDF to a MAP value of 1. The horizontal dashed line in the posterior PDF
 463 image shows the present value of k . The parameters used to construct the synthetic ETP data set were $u =$
 464 1 cm/yr and $k = 51.707$ arcsec/yr.
 465

466 To check the significance of the estimated astronomical signals, we generated $N_{\text{sim}} =$
 467 1,000 AR(2) time series with coefficients $\phi_1 = 0.84$ and $\phi_2 = -0.07$, equal to those estimated for
 468 the MAP value of u and k . The value of these coefficients are close to those of the AR noise that
 469 was added to the data ($\phi_1 = 0.8$, $\phi_2 = 0$). Figure 4 shows that the fit to all the astronomical cycles
 470 and to each individual set of cycles (climatic precession, obliquity, or eccentricity) is highly
 471 significant. Finally, the fit of an AR(2) spectrum to the periodogram of the ETP data, and the
 472 sample autocorrelation of the driving noise of the AR(2) process in the residuals e of the spectral

473 fit, are shown in Figure S1. The sample autocorrelation of the driving noise is close to that of
 474 white noise, as expected. In conclusion, TimeOptB is successful in recovering the sedimentation
 475 rate and axial precession frequency in a synthetic data set contaminated by a realistic amount of
 476 correlated noise.

477

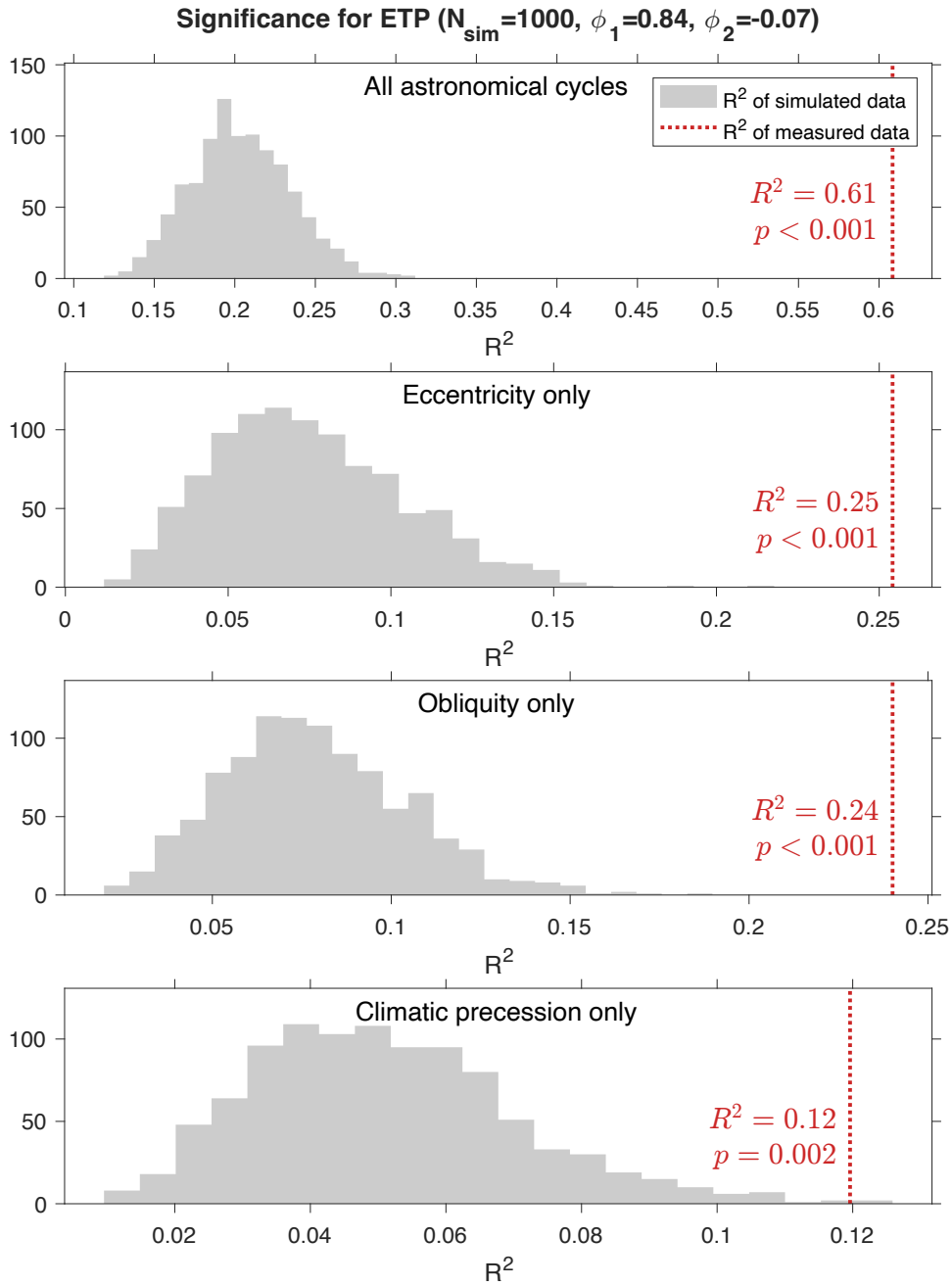


478

479

480 **Figure 3.** Fit to the synthetic ETP test stratigraphic data for the TimeOptB-derived MAP value of
 481 sedimentation rate u (0.994 cm/kyr) and axial precession frequency k (51.357 arcsec/yr). (a) Fit between
 482 measured and predicted stratigraphic data (spectral fit). (b) Fit between the envelope of the bandpassed
 483 climatic precession signal and the envelope predicted by the eccentricity frequencies (envelope fit). (c)
 484 Data periodogram (black continuous line) and frequencies of astronomical cycles (dotted vertical lines).
 485 The gray shaded area shows the frequency response of the filter used to compute the bandpassed climatic
 486 precession signal in the data (gray curve in (b)).

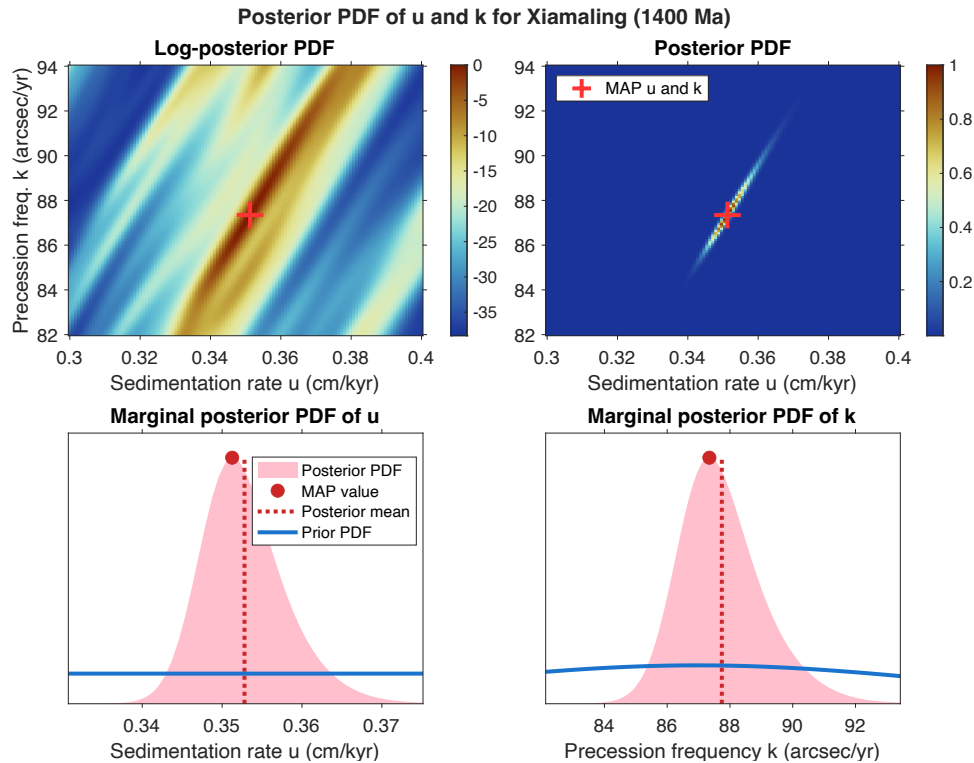
487



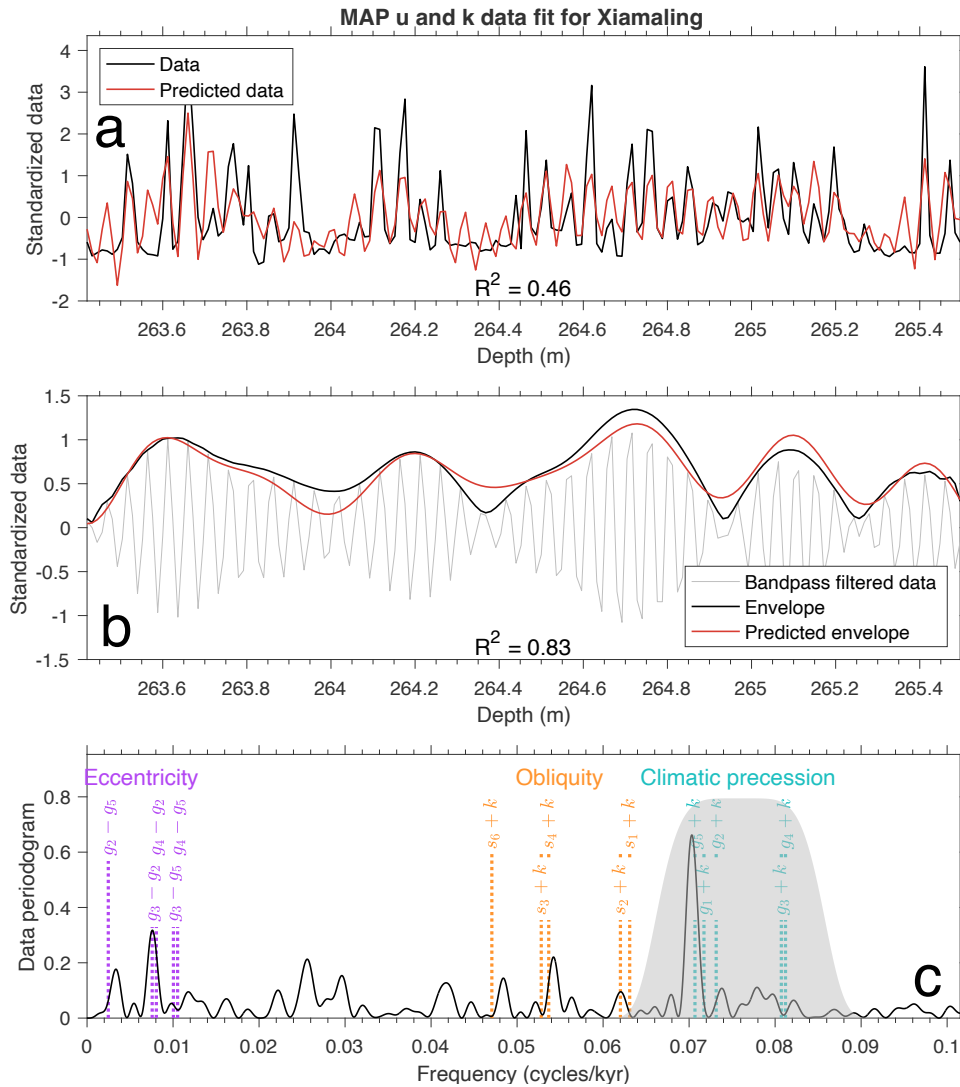
488
 489
 490
 491
 492
 493
 494
 495
 496

Figure 4. TimeOptB Monte Carlo significance testing for the synthetic ETP data set. The gray histograms show the distribution of TimeOptB R^2 values in $N_{\text{sim}} = 1000$ random AR(2) time series. The R^2 in the random time series matches or exceeds the value obtained for the synthetic ETP data set (red dotted line) at most two times out of 1000 when evaluating climatic precession alone, and does not exceed any of the simulated R^2 values when evaluating obliquity only, eccentricity only, or all of the astronomical cycles together.

497 **4.2 Xiamaling Formation (1.4 Ga)**

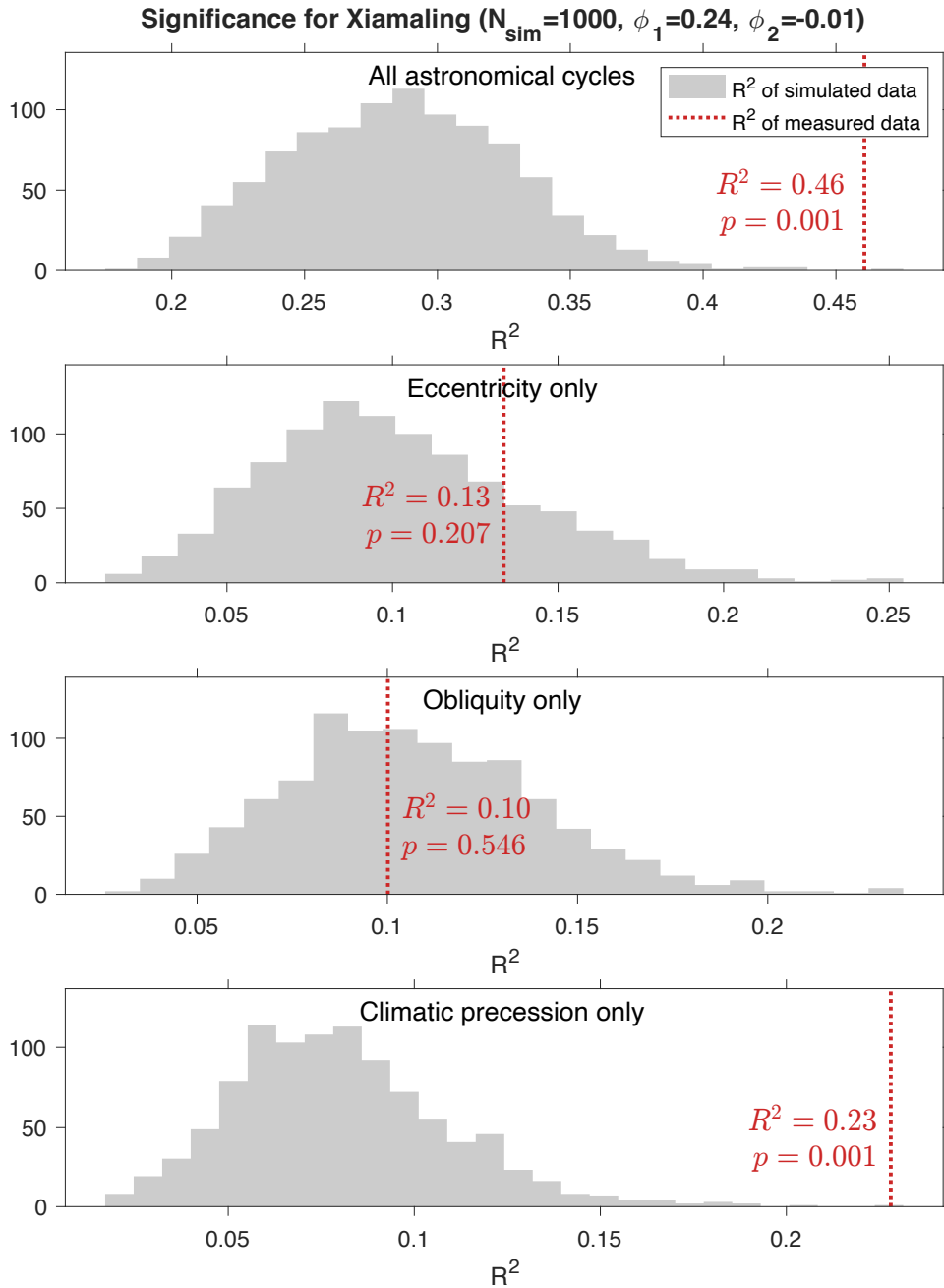
 498 We apply the TimeOptB methodology to a published Cu/Al record from the 1.4 Ga
 499 Mesoproterozoic Xiamaling Formation, North China craton (Zhang et al., 2015), one of the data
 500 sets studied by MM18. The data interval is 2 m-thick and spans about 570 kyr (for the posterior
 501 mean sedimentation rate determined below).
 502
 503

 504
 505
 506 **Figure 5.** Posterior PDFs of sedimentation rate u and axial precession frequency k obtained by TimeOptB
 507 from the Xiamaling formation data set. In the PDF images, the log-posterior PDF is normalized to a MAP
 508 value of zero and the posterior PDF to a MAP value of 1.
 509

 510 The posterior PDFs of sedimentation rate u and axial precession frequency k are shown in
 511 Figure 5. The prior PDF of k is very broad, reflecting a large uncertainty about k at 1.4 Ga, but
 512 the data are informative and result in a much narrower posterior PDF. The MAP value of u and k
 513 predict data that match closely the precession-modulated climatic precession cycles in the
 514 measured Cu/Al data, and prominent peaks in the data periodogram are near the predicted
 515 frequencies of eccentricity and climatic precession (Figure 6). The Monte Carlo significance
 516 experiments in Figure 7 support the presence of astronomical cycles, with low p -values of 0.001
 517 when all the astronomical cycles are considered or when only climatic precession is tested. The
 518 fit of an AR(2) process to the Xiamaling data is illustrated in Figure S2, and it confirms that the
 519 driving noise of the AR(2) process is nearly white noise.



520
521
522
523
524
525
526
527
528
529

Figure 6. Fit to the Xiamaling formation Cu/Al data obtained by TimeOptB for the MAP value of sedimentation rate u and axial precession frequency k (see Table 3). (a) Fit between measured and predicted stratigraphic data (spectral fit). (b) Fit between the envelope of the bandpassed climatic precession signal and the envelope predicted by the eccentricity frequencies (envelope fit). (c) Data periodogram (black continuous line) and frequencies of astronomical cycles (dotted vertical lines). The gray shaded area shows the frequency response of the filter used to compute the bandpassed climatic precession signal in the data (gray curve in (b)).



530
531
532
533
534
535
536
537

Figure 7. TimeOptB Monte Carlo significance testing for the Xiamaling formation data set. The gray histograms show the distribution of TimeOptB R^2 values in $N_{\text{sim}} = 1000$ random AR(2) time series. The R^2 values in the random time series are all clearly lower than the value obtained for the measured data (red dotted line) when considering all the astronomical cycles or the climatic precession cycles only.

538 **Table 3.** Results of TimeOptB and TimeOptBMCMC for the Xiamaling Formation Cu/Al and Walvis
 539 Ridge a* data. MAP = Maximum a posteriori, value of the parameter at the mode of the posterior PDF.
 540

Xiamaling Formation (1.4 Ga)					
	MAP value	Posterior mean	Posterior σ	95% credible interval	Method
Sedimentation rate u (cm/kyr)	0.351 0.353	0.353 0.352	0.00540 0.00541	0.343-0.365 0.343-0.364	TimeOptB TimeOptBMCMC
Axial precession frequency k (arcsec/yr)	87.34 87.82	87.74 87.49	1.38 1.38	85.37-90.81 85.21-90.61	TimeOptB TimeOptBMCMC
Semi-major axis of lunar orbit a (Earth radii)		53.08	0.25		Based on TimeOptB posterior mean and σ
LOD (hrs)		18.47	0.22		
Walvis Ridge (55 Ma)					
	MAP value	Posterior mean	Posterior σ	95% credible interval	Method
Sedimentation rate u (cm/kyr)	1.308 1.311	1.309 1.310	0.00605 0.00620	1.297-1.320 1.299-1.322	TimeOptB TimeOptBMCMC
Axial precession frequency k (arcsec/yr)	51.15 51.31	51.25 51.29	0.29 0.29	50.70-51.81 50.75-51.85	TimeOptB TimeOptBMCMC
Semi-major axis of lunar orbit a (Earth radii)		60.07	0.12		Based on TimeOptB posterior mean and σ
LOD (hrs)		23.75	0.11		

541
542

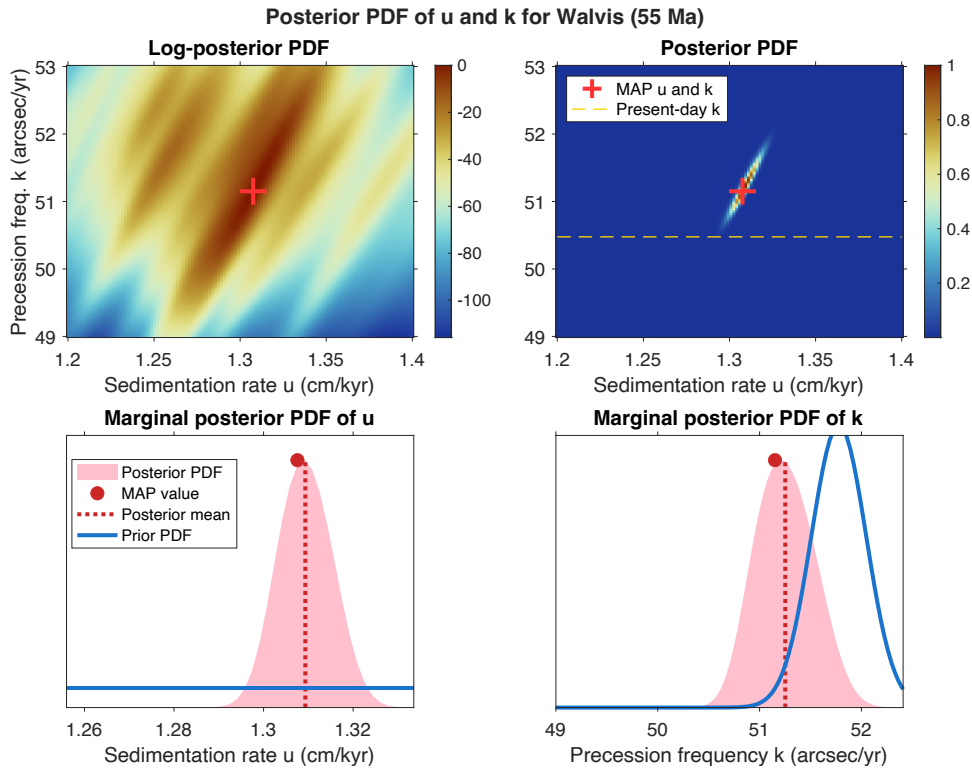
543 **4.3 Walvis Ridge ODP Site 1262 (55 Ma)**

544 Another case study for the TimeOptB methodology uses a record of reflectivity data (a*,
 545 red/green) measured on Eocene-age sediments cored at ODP Site 1262, Walvis Ridge, South
 546 Atlantic (Zachos et al., 2004), which was also studied by MM18. We refer to that study and
 547 Zachos et al. (2004) for details about the a* data set. The data interval is 21 m-thick and spans
 548 about 1.6 Myr (for the posterior mean sedimentation rate determined below).

549 The posterior PDFs of sedimentation rate u and axial precession frequency k are
 550 illustrated in Figure 8. At 55 Ma, the prior PDF of k is much narrower than in the
 551 Mesoproterozoic example; the Walvis Ridge data point to values of k that are somewhat lower
 552 than those in the prior PDF. As in the previous example, the MAP values of u and k result in
 553 predicted data that closely reproduce the observed precession-modulated climatic precession
 554 cycles, and the predicted frequencies of eccentricity and climatic precession coincide with the
 555 highest peaks in the data periodogram (Figure 9). The periodogram of the Walvis record shows
 556 very little power at the expected frequencies of obliquity, and the Monte Carlo significance
 557 experiments show high significance for all astronomical cycles, for eccentricity only, and for
 558 climatic precession only (Figure 10). In contrast, the power of cycles at the obliquity frequencies
 559 in the random simulated data is always greater than in the measured data; the reason is that the
 560 obliquity frequency band (0.019-0.035 cycles/kyr) of the periodogram of the Walvis data has
 561 markedly lower power than that of the fitted AR(2) process (Figure S3a). Figure S3b shows that
 562 the driving noise of the fitted AR(2) process is nearly white noise.

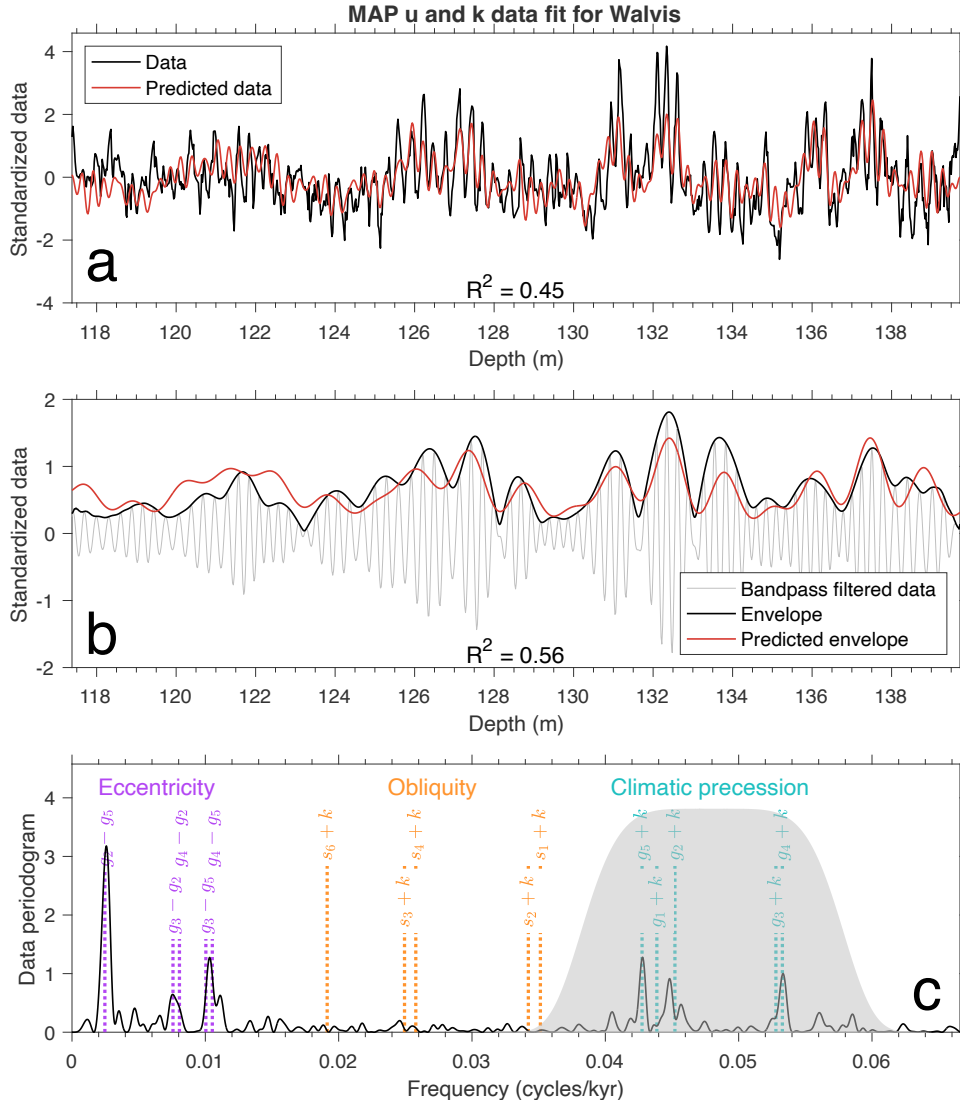
563

564
565



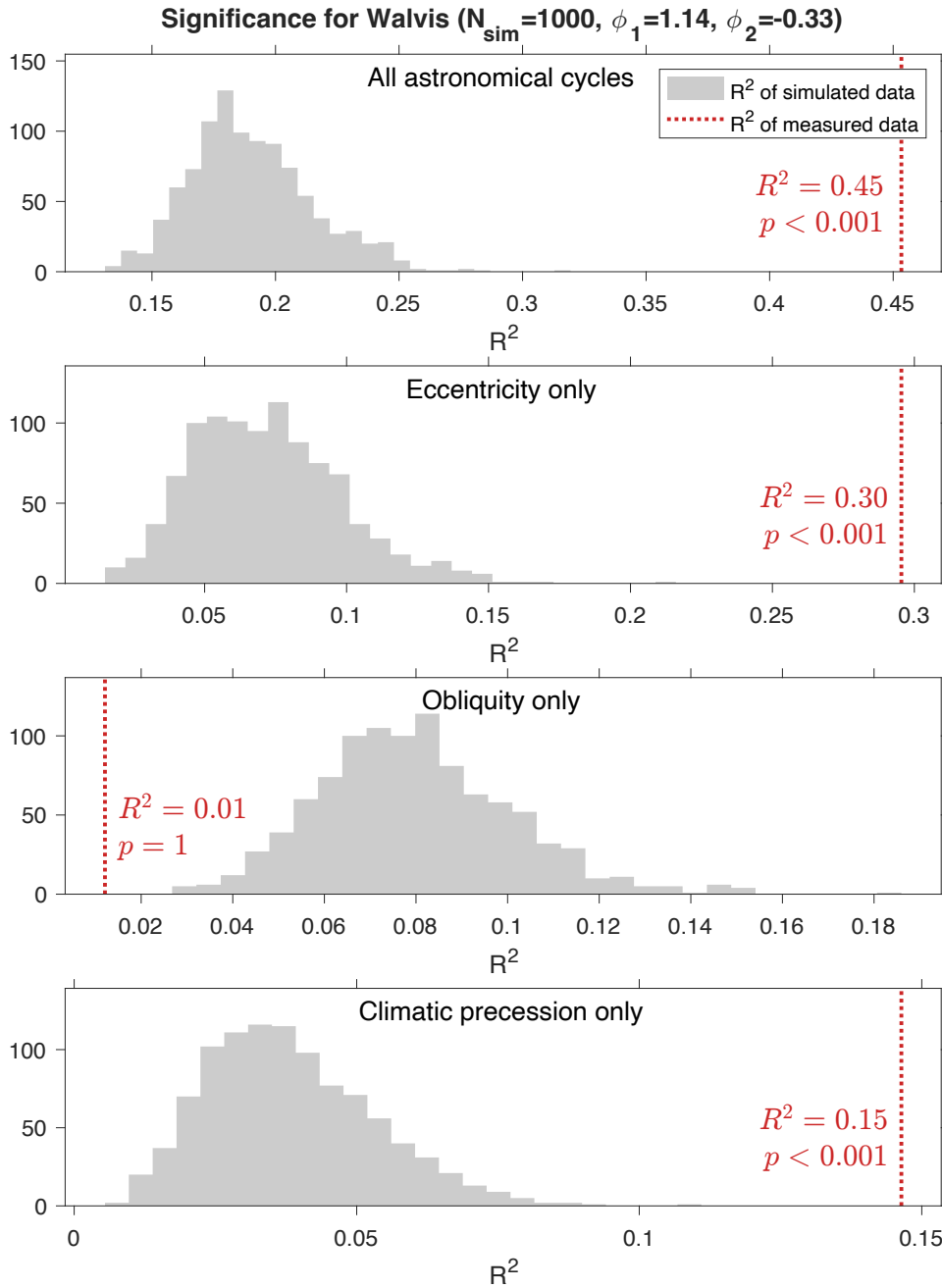
566
567
568
569
570
571
572

Figure 8. Posterior PDFs of sedimentation rate u and axial precession frequency k obtained by TimeOptB from the Walvis Ridge a^* data set. In the PDF images, the log-posterior PDF is normalized to a MAP value of zero and the posterior PDF to a MAP value of 1. The horizontal dashed line in the posterior PDF image shows the present value of k .



573
 574
 575
 576
 577
 578
 579
 580
 581
 582
 583

Figure 9. Fit to the Walvis Ridge a^* data obtained by TimeOptB for the MAP value of sedimentation rate u and axial precession frequency k (see Table 3). (a) Fit between measured and predicted stratigraphic data (spectral fit). (b) Fit between the envelope of the bandpassed climatic precession signal and the envelope predicted by the eccentricity frequencies (envelope fit). (c) Data periodogram (black continuous line) and frequencies of astronomical cycles (dotted vertical lines). The gray shaded area shows the frequency response of the filter used to compute the bandpassed climatic precession signal in the data (gray curve in (b)).



584
585
586
587
588
589
590
591
592

Figure 10. TimeOptB Monte Carlo significance testing for the Walvis Ridge data set. The gray histograms show the distribution of TimeOptB R^2 values in $N_{\text{sim}} = 1000$ random AR(2) time series. The R^2 values in the random time series are clearly lower than the value obtained for the measured data (red dotted line) when considering all the astronomical cycles, the eccentricity cycles only, or the climatic precession cycles only.

593 **5 TimeOptBMCMC methodology**

594 In the TimeOptB method, the only variable parameters are the sedimentation rate u and
 595 axial precession frequency k , while the fundamental Solar system frequencies g_i and s_i are kept
 596 fixed at their prior mean values. As noted in the Introduction, however, we also aim to use
 597 stratigraphic records to constrain the history of variation in the frequencies g_i and s_i and in long-
 598 term astronomical periodicities such as the $g_4 - g_3$ cycle. The method we present here is an
 599 offshoot of the TimeOptMCMC procedure of MM18, which sampled the posterior PDF of five
 600 fundamental Solar system frequencies g_i , axial precession frequency k , and sedimentation rate u
 601 (plus some hyperparameters, discussed below). In TimeOptBMCMC we add the five Solar
 602 system frequencies s_i to determine the posterior PDF of the full twelve-parameter vector in
 603 Equation 1.

604 Whereas in TimeOptB the value of the posterior PDF was calculated systematically over
 605 a grid of two parameters (u and k), the same strategy cannot be used for twelve parameters.
 606 Evaluating the PDF over a grid of M points for each parameter (say, $M = 100$) would require M^{12}
 607 calculations, which is entirely impractical. In contrast, MCMC algorithms perform a random
 608 walk that concentrates on the high-posterior probability region of the parameter space and are
 609 designed to return a sample distributed as in the posterior PDF. General treatments of MCMC in
 610 the statistical literature can be found in Gilks et al. (1996) and Brooks et al. (2011); examples of
 611 applications to geophysical inverse problems are in Malinverno (2002), Sambridge & Mosegaard
 612 (2002), Piana Agostinetti & Malinverno (2010), and Sen & Stoffa (2013).

613 TimeOptBMCMC uses a Metropolis-within-Gibbs algorithm (originally described by
 614 Metropolis et al., 1953): in each step of the random walk, a candidate parameter vector is
 615 obtained by adding to one of the parameters a random value chosen from a proposal PDF (e.g., a
 616 zero-mean normal PDF). The candidate is then accepted with a probability that depends on the
 617 ratio of the posterior PDFs of the candidate and the current parameter vector. This simple
 618 strategy will asymptotically return a sample of parameter vectors distributed as in the posterior
 619 PDF.

620 An outstanding issue in implementing a Metropolis algorithm is how to choose the scale
 621 parameter of the proposal PDF (e.g., the standard deviation of a normal PDF). If this scale is set
 622 too large, most candidates will not be accepted; if too small, the probability of acceptance will be
 623 large but the random walker will diffuse too slowly through the parameter space. In both cases, it
 624 will take a long time to explore the high-posterior probability region. In TimeOptBMCMC, we
 625 apply an adaptive Metropolis-within-Gibbs algorithm (Haario et al., 2001; Roberts & Rosenthal,
 626 2009), where parameters are changed one at a time and the standard deviation of the normal
 627 proposal PDF of each parameter is progressively adjusted from a starting value to maintain a
 628 target rate of acceptance of 0.44, which has been shown to be optimal in this case (Roberts &
 629 Rosenthal, 2001). This is a significant improvement over TimeOptMCMC (MM18), which
 630 required a laborious initial experimentation, running a number of MCMC sampling chains to
 631 adjust the scale parameters of the proposal PDFs, often resulting in acceptance rates that were
 632 not ideal, which increased the computation time.

633 Another key difference is that TimeOptBMCMC applies an empirical Bayes approach to
 634 estimate directly from the data a best value of the hyperparameters that control the form of the
 635 covariance matrix of the residuals in the likelihood function for the spectral fit (two AR process
 636 coefficients and the residual variance; see the Supporting Information). TimeOptMCMC instead

637 characterized the residuals with an AR(1) process, which is not always appropriate (e.g., the
 638 spectral fit residuals in the Walvis Ridge data required a nonzero coefficient ϕ_2 ; see Figure S3),
 639 and included the AR process coefficient and the variance of the residuals as variable
 640 hyperparameters in the inversion, which adds to the computational cost of the MM18 procedure.

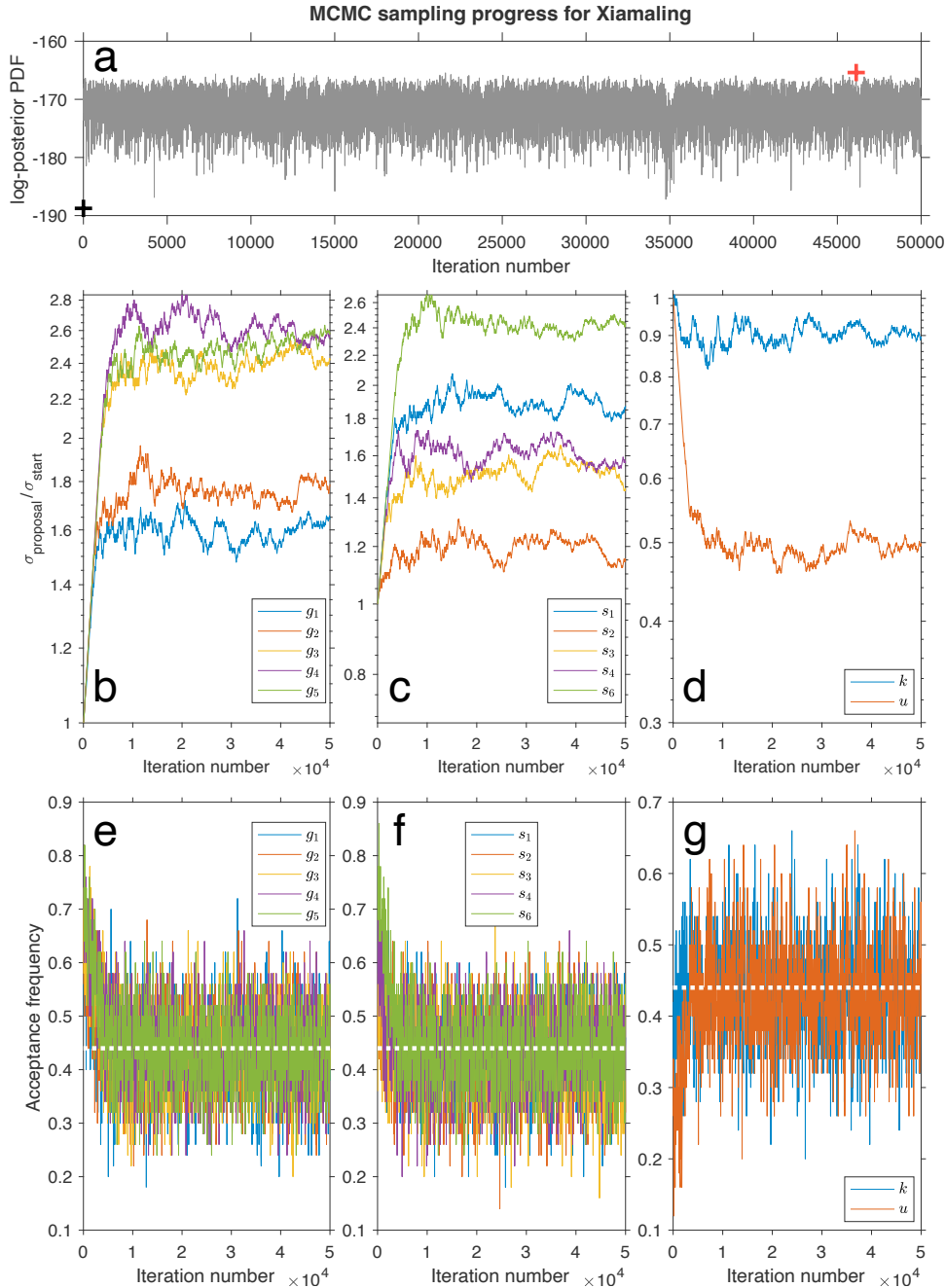
641 **6 TimeOptBMCMC example results**

642 **6.1 Xiamaling Formation (1.4 Ga)**

643 The progress of TimeOptBMCMC in sampling the posterior PDF of all the parameters
 644 for the Xiamaling Cu/Al data is illustrated in Figure 11. The chain is started from the prior mean
 645 value of the Solar system frequencies g_i and s_i , axial precession frequency k , and sedimentation
 646 rate u (whose prior PDF is a uniform distribution between 0.3 and 0.4 cm/kyr) and proceeds for
 647 50,000 iterations. The value of the posterior PDF rises very quickly at the start of the MCMC
 648 sampling chain and then fluctuates within the high-probability region (Figure 11a). The initial
 649 values of the standard deviation of each proposal PDF are set to the prior standard deviation of
 650 the astronomical frequencies (with an upper limit for the proposal standard deviation of k , where
 651 the prior standard deviation can be very large) and to a small fraction of the prior mean of u . The
 652 progressive adjustment of the proposal PDF standard deviations (Figure 11b-d) and the
 653 corresponding change in the frequency of acceptance (Figure 11e-g) show that after about 5,000
 654 iterations the proposal standard deviations and the frequency of acceptance for each parameter
 655 fluctuate around a constant value, with an average frequency of acceptance around the optimal
 656 value of 0.44.

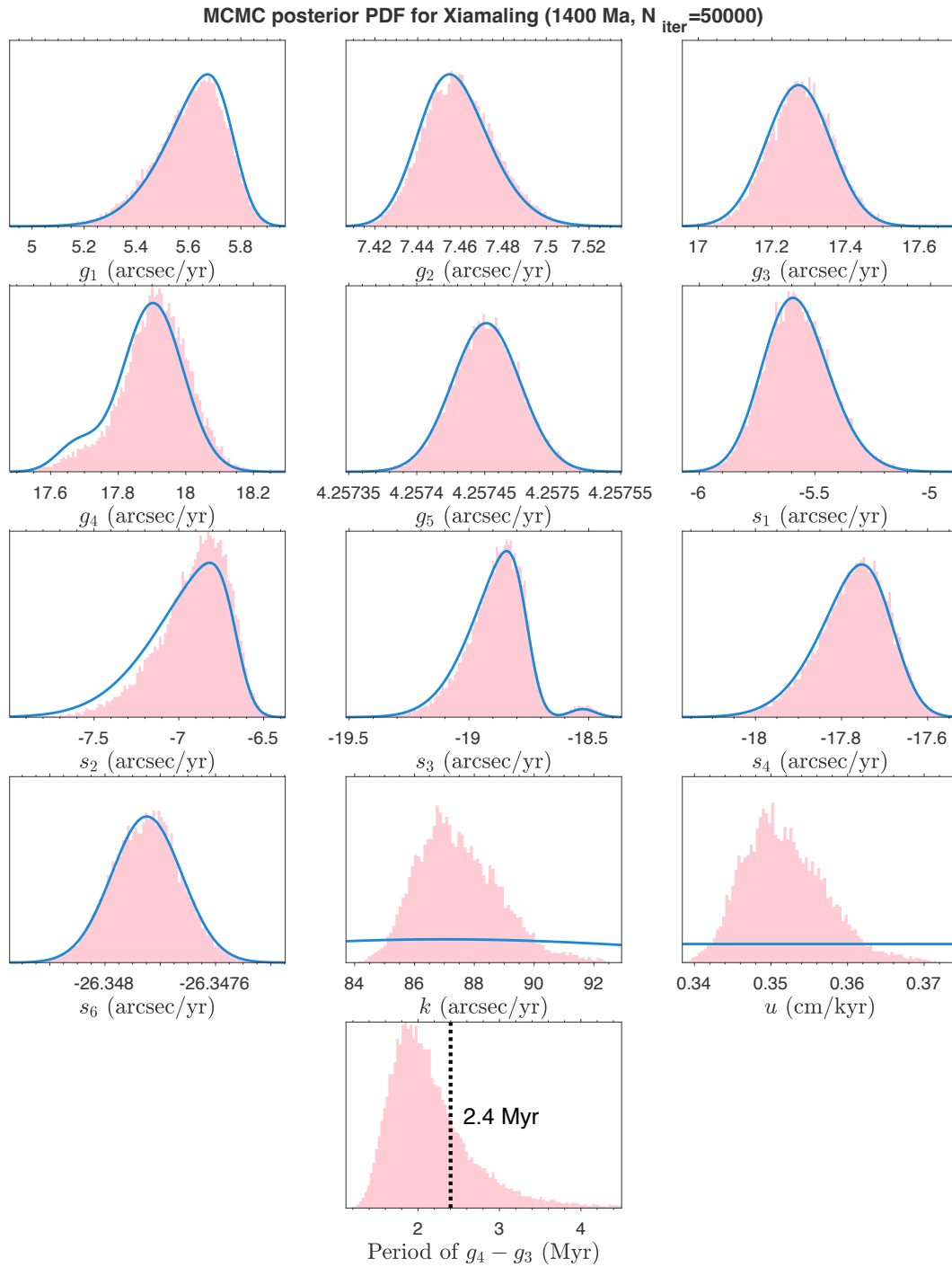
657 Figure 12 compares the prior PDFs of each parameter to the histograms of the values
 658 sampled by TimeOptBMCMC, which approximate each posterior PDF. The prior and posterior
 659 PDFs of the g_i and s_i frequencies are very similar, whereas the data clearly constrain the posterior
 660 values of k and u to a much narrower interval than in the prior PDF. Figure 12 also shows the
 661 posterior histogram of the period corresponding to the $g_4 - g_3$ frequency, which has a sizable
 662 posterior uncertainty (the central 95% interval of the posterior PDF is 1.47-3.78 Myr). The
 663 $g_4 - g_3$ frequency has a large uncertainty because it is estimated from a relatively short record
 664 that only spans a ~ 570 kyr interval. The present day value of the $g_4 - g_3$ period (2.4 Myr) is
 665 within the range consistent with the Xiamaling data at 1.4 Ga.

666 The posterior correlations between the parameters are generally small, with the exception
 667 of a strong positive correlation between u and k (Figure S4), which is the same positive
 668 correlation obtained in the TimeOptB results for the Xiamaling formation Cu/Al data (Figure 5).
 669 In contrast, the g_i and s_i frequencies are not correlated a posteriori with the sedimentation rate u
 670 because their prior variances are much smaller than that of k (Figure 1) so that they cannot vary
 671 over an interval large enough to relate to differences in u . In fact, the sedimentation rate is
 672 mostly constrained by eccentricity frequencies $g_i - g_j$ in the spectral and envelope fit, which have
 673 a small prior variability. The marginal posterior PDFs of u and k obtained by TimeOptB (g_i and
 674 s_i fixed to their prior mean values) and TimeOptBMCMC (g_i and s_i variable) are also very
 675 similar (compare Figures 5 and 12 and the posterior PDF statistics in Table 3). Finally, the MAP
 676 value of the parameters sampled by TimeOptBMCMC results in predicted data that are
 677 essentially the same as those obtained by TimeOptB (compare Figures 6 and S5).



678
679

680 **Figure 11.** Progress of TimeOptBMCMC sampling for the Xiamaling formation Cu/Al data set over
681 50,000 iterations. (a) Value of the log-posterior PDF for the sampled model parameter vectors. The black
682 cross is the starting value and the red cross the MAP. (b, c, d) Standard deviation of the proposal PDF (as
683 a ratio over the starting value) for each model parameter. (e, f, g) Frequency of acceptance of the
684 proposed steps in the MCMC random walk. The adaptive Metropolis algorithm used in TimeOptBMCMC
685 adjusts the standard deviations of the proposal PDF to keep the frequency of acceptance around the
686 optimal value of 0.44 for all model parameters (white horizontal dotted line).
687



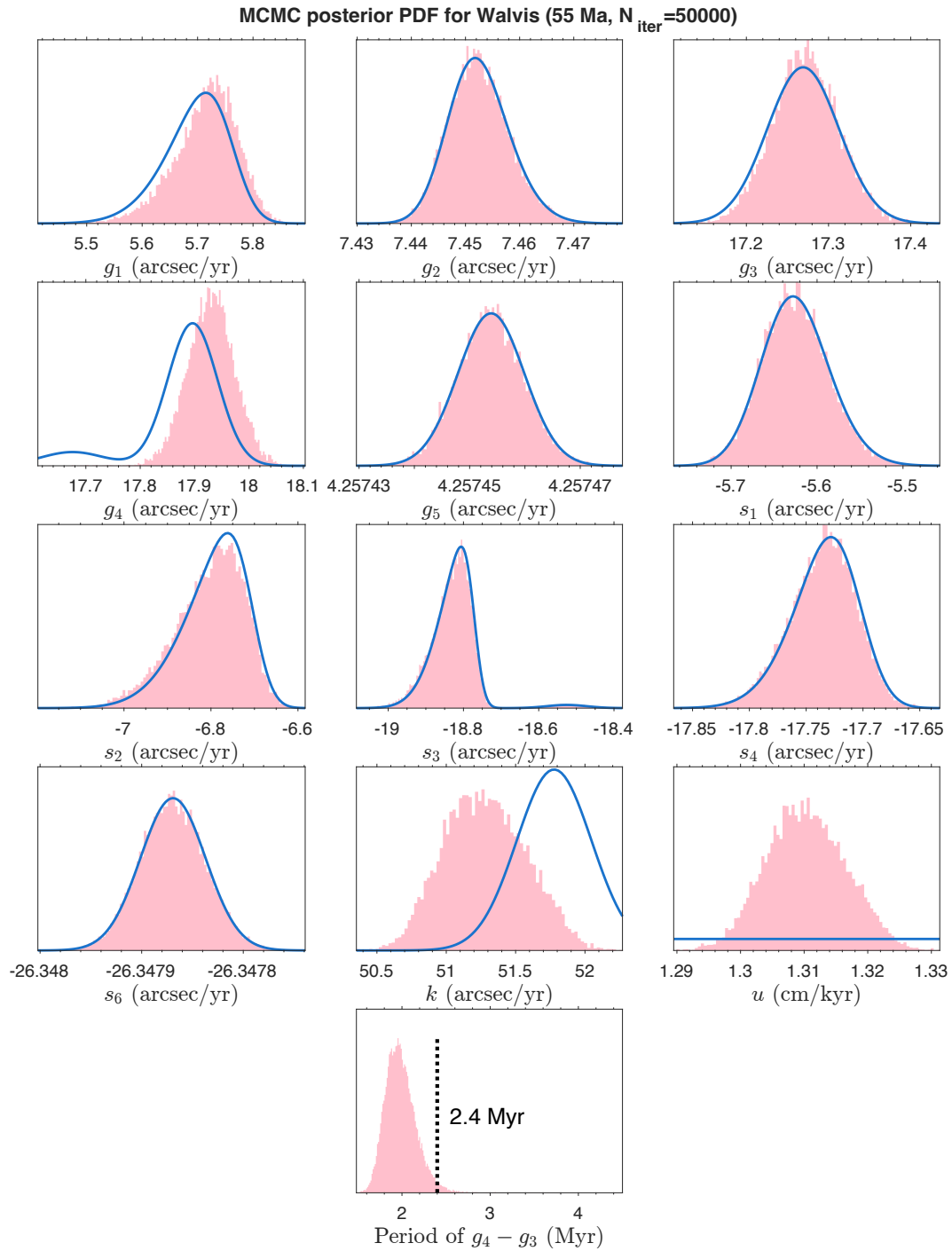
688
689
690
691
692
693
694
695

Figure 12. Histograms of posterior model parameter values sampled by TimeOptBMCMC for the Xiamaling formation Cu/Al data set over 50,000 iterations (light red) compared to the prior PDFs (blue curves). The bottom panel shows the posterior distribution of sampled $g_4 - g_3$ periods compared to the present day value of 2.4 Myr (vertical dotted black line).

696 **6.2 Walvis Ridge ODP Site 1262 (55 Ma)**

697 The progress of TimeOptBMCMC in sampling the posterior PDF for the Walvis Ridge
698 a* data (Figure S6) is very similar to that seen for the Xiamaling formation Cu/Al data (Figure
699 11). The prior and posterior PDFs of g_i and s_i are also similar, with the exception of g_4 , whose
700 posterior PDF is shifted towards higher frequencies (Figure 13). As a result, the posterior PDF of
701 the $g_4 - g_3$ period is shifted toward shorter periods, and the present day value of 2.4 Myr is in the
702 tail of the posterior PDF (the central 95% interval of the posterior PDF is 1.69-2.38 Myr).

703 As seen for the Xiamaling formation Cu/Al data set, the posterior correlations in the
704 Walvis Ridge a* results are generally small, except for the strong positive correlation between u
705 and k (Figure S7) that was also seen in the TimeOptB results (Figure 8). Again, the marginal
706 posterior PDFs of u and k obtained by TimeOptB (g_i and s_i fixed) and TimeOptBMCMC (g_i and
707 s_i variable) are very similar (compare Figures 8 and 13 and posterior statistics in Table 3). The
708 data predicted by the MAP value obtained by TimeOptB and TimeOptBMCMC are also
709 essentially identical (compare Figures 9 and S8).



710
711
712
713
714
715
716

Figure 13. Histograms of posterior model parameter values sampled by TimeOptBMCMC for the Walvis Ridge formation a* data set over 50,000 iterations (light red) compared to the prior PDFs (blue curves). The bottom panel shows the posterior distribution of sampled $g_4 - g_3$ periods compared to the present day value of 2.4 Myr (vertical dotted black line).

717 **7 Lunar distance and LOD from an estimate of axial precession frequency k**

718 The axial precession frequency k depends on both the lunar distance a (semi-major axis
719 of the Moon orbit) and the Earth spin rate ω (or equivalently, LOD); e.g., see Equation 7 of
720 Berger & Loutre (1994) or Equation 4.14 of Laskar (2020). Therefore, obtaining values of lunar
721 distance and LOD from an estimate of k requires an additional constraint, which is usually
722 provided by the conservation of angular momentum in the Earth-Moon system (e.g., MM18;
723 Lantink et al., 2022).

724 To estimate lunar distance and LOD from k , we apply two equations derived from
725 Equations 6 and 7 of Walker & Zahnle (1986). The first equation gives the relationship between
726 the axial precession frequency k , lunar distance a , and Earth spin rate ω as

$$727 \quad \frac{\omega(t)}{\omega(0)} = \frac{k(t)}{k(0)} \frac{K+1}{K + \left[\frac{a(t)}{a(0)}\right]^{-3}}, \quad (5)$$

728 where $k(t)/k(0)$, $a(t)/a(0)$, and $\omega(t)/\omega(0)$ are ratios between values at age t and present day values,
729 and K is a dimensionless constant. Equation 5 can be derived from the fundamental equation for
730 the precession frequency k (e.g., Equation 7 of Berger & Loutre, 1994) for circular, coplanar
731 orbits and a constant obliquity ε . The precession frequency equation also contains the dynamic
732 ellipticity $H = (C - A)/C$, where C and A are the Earth's moments of inertia about polar and
733 equatorial axes, respectively. H will change as the Earth changes its shape due to variations in
734 spin rate ω , and Equation 5 is derived assuming that over long time scales the Earth deforms as a
735 fluid in hydrostatic equilibrium so that H is proportional to the square of ω (Equation 5.3.2 of
736 Munk & MacDonald, 1960). The dynamic ellipticity H can also change with changes in mass
737 distribution within the Earth, e.g., because of the effects of glaciations or mantle convection. The
738 resulting changes in H , however, are relatively small; they do not exceed about 0.25% for
739 glaciation effects in the last 47 Ma (Figure 3 of Farhat, Laskar, et al., 2022) or for mantle
740 convection in the last 50 Ma (Figure 1A of Ghelichkhan et al., 2021). In contrast, the progressive
741 decrease in the Earth spin rate due to tidal dissipation had much greater effects on H over
742 geologic time scales. For example, a simple calculation of the effect of tidal dissipation
743 (Equation 4.19 of Laskar, 2020) gives a ω^2 that was 3.2% greater than the present at 50 Ma,
744 6.6% greater at 100 Ma, and 22.5% greater at 300 Ma. This substantial systematic change
745 justifies assuming that over time scales of tens of Myr the dynamic ellipticity H is primarily
746 controlled by the progressive slowing down of the Earth spin rate.

747 The second equation is the relationship between lunar distance and LOD that conserves
748 angular momentum in the Earth-Moon system:

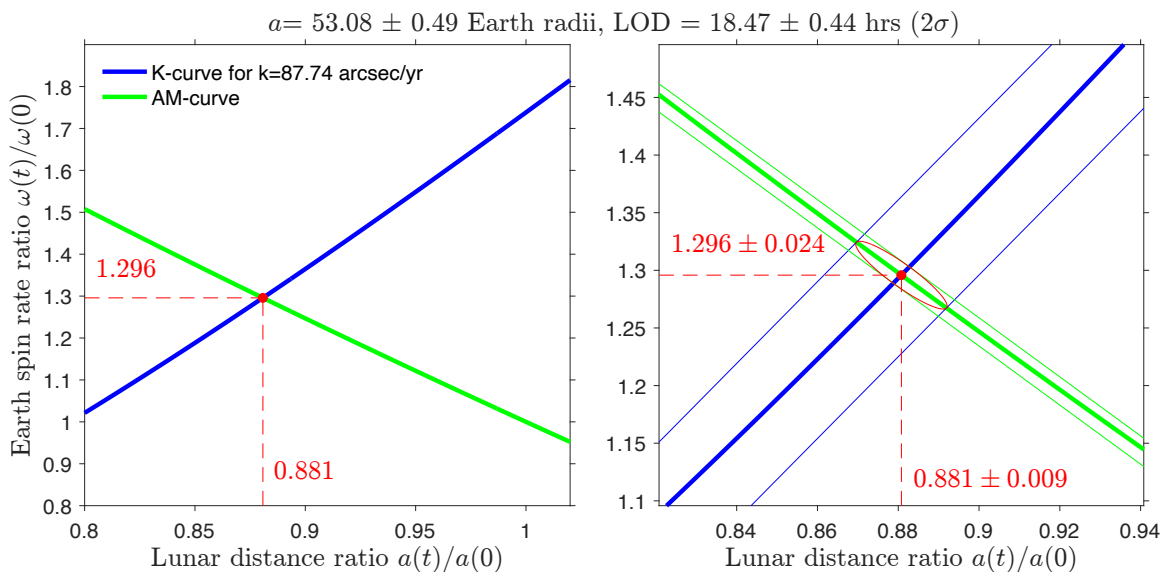
$$749 \quad \frac{\omega(t)}{\omega(0)} = 1 + A - A \left[\frac{a(t)}{a(0)}\right]^{1/2}. \quad (6)$$

750 The values of the dimensionless constants in Equations 5 and 6 were originally given by Walker
751 & Zahnle (1986) as $K = 0.465$ and $A = 4.87$. Here we adjust the values of these dimensionless
752 constants to account for effects that were originally neglected in Walker & Zahnle (1986): the
753 systematic increase of obliquity ε during geologic time and the effect of solar ocean tides on the
754 slowdown of the Earth spin rate. These adjustments were done by comparing the predictions of
755 Equations 5 and 6 with the values of a , ω , and k calculated over the last 3.3 Ga by Farhat,
756 Auclair-Desrotour, et al. (2022). The updated values of the constants are $K = 0.358$ and $A = 4.81$;
757 details are in the Supporting Information.

758 The two relationships above define two curves of $\omega(t)/\omega(0)$ as a function of $a(t)/a(0)$: a
 759 “K-curve” that corresponds to a given value of $k(t)/k(0)$ (Equation 5) and an “AM-curve” that
 760 conserves angular momentum (Equation 6). The intersection of these two curves, illustrated in
 761 Figure 14a, gives the values of past lunar distance a , Earth spin rate ω , and LOD. The
 762 Supporting Information describes a simple way to obtain the intersection from a polynomial fit.

763 An uncertainty in the estimates of a and LOD can be calculated on the basis of the
 764 uncertainties in the K-curve and AM-curve and of the uncertainty in the value of k estimated
 765 from cyclostratigraphic data; see Figure 14b for an illustration and the Supporting Information
 766 for details of the calculation. The approach outlined above provides an accurate and quick means
 767 to obtain a , LOD, and their uncertainties from an estimate of k , and the results for the examples
 768 evaluated here are listed in Table 3.

769



770

771

772 **Figure 14.** Ratio $\omega(t)/\omega(0)$ between the Earth’s spin rate at age t and the present day value as a function
 773 of the ratio of the lunar distances $a(t)/a(0)$. (a) The blue curve (K-curve; Equation 5) shows the
 774 relationship for the axial precession frequency $k(t)$ estimated from the Xiamaling formation Cu/Al data set
 775 ($t = 1.4$ Ga) and the green curve (AM-curve; Equation 6) the relationship that conserves the Earth-Moon
 776 angular momentum. The red dot at the intersection of the two curves gives the values of $a(t)/a(0)$ and
 777 $\omega(t)/\omega(0)$ at age t . (b) Thin blue and green lines are the 95% contours of normal distributions that describe
 778 the uncertainties of the K-curve and AM-curve, respectively, and the red ellipse is the 95% contour that
 779 defines the uncertainty of the intersection (see the Supporting Information for details).

780

781 8 Discussion

782 8.1 Estimating axial precession frequency k

783 The case studies evaluated here show that TimeOptB and TimeOptBMCMC are effective
 784 in estimating a value for the precession frequency k from stratigraphic data. The key requirement
 785 is that the data should display clear eccentricity cycles (which do not depend on k) and clear
 786 climatic precession and/or obliquity cycles (which depend on k). The difference in the observed
 787 frequencies of eccentricity and those of climatic precession/obliquity allows for estimating k .

788 Thus, to estimate k it is important that sizable astronomical cycles are observed in the
 789 periodogram plots for eccentricity and either precession or obliquity (Figures 3, 6, and 9). The
 790 TimeOptB significance test should also weed out cases where stratigraphic sequences do not
 791 contain significant astronomical cycles (Figures 4, 7, and 10). It should be noted that the methods
 792 presented here will not work appropriately if sedimentation rate is not relatively constant within
 793 the analyzed stratigraphic interval, which requires careful selection of cyclostratigraphic data sets
 794 or portions thereof (more on the sedimentation rate assumption below). Considering these
 795 limitations, there should be many stratigraphic data sets that can return valid estimates of the past
 796 axial precession frequency. In addition to providing valuable information on the evolution of
 797 lunar distance, LOD, and tidal dissipation, past estimates of k will improve the accuracy of
 798 astrochronologies based on climatic precession and obliquity cycles in data.

799 The results in Table 3 supersede those obtained for the Xiamaling formation and Walvis
 800 Ridge in MM18. The differences are minor, and in both cases the posterior PDFs of k and u in
 801 this study overlap with those in MM18. The posterior PDFs of k in the Xiamaling formation are
 802 not identical with MM18 because TimeOptB and TimeOptBMCMC include the fit to obliquity
 803 components, which results in a small increase in k (the posterior mean changes from 85.79
 804 arcsec/yr in MM18 to 87.74 arcsec/yr in Table 3). The posterior PDF of k in the Walvis Ridge
 805 data is very close to that in MM18 even though the prior PDF was different between the studies.

806 The posterior PDFs of u and k obtained by TimeOptB and TimeOptBMCMC are similar
 807 in both the Xiamaling Formation Cu/Al and Walvis Ridge a* data sets (Figures 5, 8, 12, 13, and
 808 Table 3). Thus, in these two case studies, letting the g_i and s_i frequencies be variable parameters
 809 does not lead to different estimates of u and k or to a substantially improved fit of the results
 810 (Figures 6, 9, S5, S8).

811 **8.2 Estimating Solar system fundamental frequencies g_i and s_i**

812 The posterior PDFs of the g_i and s_i frequencies sampled by TimeOptBMCMC are
 813 generally close to the respective priors, with the exception of g_4 in the Walvis Ridge a* data set.
 814 When astronomical cycles are well expressed in the data, this result shows that
 815 TimeOptBMCMC can constrain the values of Solar system fundamental frequencies. The past
 816 Solar system frequencies inferred from stratigraphic data will have inherent uncertainties. In
 817 practice, long-period cycles such as $g_4 - g_3$ will not be reconstructed with high accuracy from
 818 stratigraphic records of relatively short duration, but nonetheless the range of their possible
 819 values can be estimated by TimeOptBMCMC. For example, although the posterior PDF of the
 820 $g_4 - g_3$ period in the Walvis Ridge record (55 Ma) spans a broad interval, the results in Figure 13
 821 suggest a $g_4 - g_3$ period that is shorter than the present 2.4 Myr. For comparison, Zeebe &
 822 Lourens (2019) also found that the Solar system solution that best fit the Walvis Ridge data
 823 displayed a decrease in the $g_4 - g_3$ period to ~ 1.5 Myr at ages older than 50 Ma (though 1.5 Myr
 824 is at the very low end of the posterior PDF of the $g_4 - g_3$ period in Figure 13).

825 A suggested practical procedure is to run TimeOptB first on a data set, including the
 826 Monte Carlo significance experiments to support the presence of astronomical cycles in the data.
 827 If there is evidence for astronomical cycles in the data, a TimeOptBMCMC run can show
 828 whether the sampled values of the Solar system fundamental frequencies are distributed as in the
 829 prior PDF, meaning that the data are not informative (as in the case of the Xiamaling formation
 830 Cu/Al data set) or whether there are differences from the prior that highlight past variations (as
 831 for g_4 and $g_4 - g_3$ in the Walvis Ridge a* data set).

832 **8.3 Assumption: constant sedimentation rate**

833 A key assumption in TimeOptB and TimeOptBMCMC is that the sedimentation rate was
 834 constant in the studied stratigraphic interval. A preliminary moving window power spectral
 835 analysis or wavelet-based analysis can indicate whether prominent cycles have nearly constant
 836 spatial frequencies as predicted by a constant sedimentation rate. This means that suitable data
 837 sets will likely span a relatively short time interval, and there will be a tradeoff between the need
 838 to have a long enough record of eccentricity cycles and the requirement of a constant
 839 sedimentation rate. Also, the strategy presented here will not be reliable if astronomical signals
 840 are distorted by large cyclic changes in sedimentation rate driven by the effects of particular
 841 astronomical cycles (e.g., Herbert, 1994).

842 Even when sedimentation rate is nearly constant over the interval studied, the examples
 843 presented here show that any error in estimating sedimentation rate u will result in the same error
 844 in axial precession frequency k : a sedimentation rate overestimated by 1% means k will be
 845 overestimated by 1% (see the discussion of the ETP data set results in Figure 2). There is no way
 846 to know k within a small fraction of its value unless the sedimentation rate, or more generally the
 847 time-stratigraphic depth relationship, is also known within that same small fraction. As
 848 stratigraphic data invariably contain variations unrelated to astronomical forcing (“geological
 849 noise;” Meyers, 2019), the time-depth relationship can be determined only approximately. This
 850 is a fundamental issue at the root of cyclostratigraphy and astrochronology applications, and it
 851 cannot be solved by methodological improvements. On the other hand, methods such as those
 852 presented here can quantify the resulting uncertainty and highlight the value and the limitations
 853 of conclusions drawn from the analysis of astronomical cycles in stratigraphic records.

854 **8.4 Assumption: constant Earth-Moon angular momentum**

855 As noted earlier, the axial precession frequency k depends on both lunar distance a and
 856 LOD. Estimating both a and LOD on the basis of k therefore requires an additional constraint,
 857 which we impose by using the common assumption that the Earth-Moon angular momentum
 858 remained constant throughout Earth’s history (with a correction due to the small effect of Solar
 859 ocean tides in slowing down the Earth’s rotation).

860 In contrast, Zahnle & Walker (1987) and Bartlett & Stevenson (2016) proposed that when
 861 LOD decreased to ~21 hrs in the Proterozoic, a solar atmospheric tide became resonant with the
 862 Earth’s spin rate and counteracted the effect of the lunar ocean tide, maintaining a constant Earth
 863 spin rate for a prolonged duration (between ~2 Ga and ~1 Ga; Bartlett & Stevenson, 2016).
 864 During this interval, the lunar ocean tide would still have resulted in a torque that moved the
 865 Moon to a higher orbit, so that the total angular momentum of the Earth-Moon system would
 866 have increased through time by as much as 10-20%, extracting angular momentum from the
 867 Earth’s orbit around the Sun (Zahnle & Walker, 1987). Our results give some information on the
 868 possible size of the change in the Earth-Moon angular momentum if this were the case: taking
 869 the value of $k(t)$ estimated from the Xiamaling formation Cu/Al record and assuming that LOD
 870 was 21 hours rather than keeping the Earth-Moon angular momentum to its present value,
 871 Equation 5 gives a ratio $a(t)/a(0) = 0.834$. If the Earth was spinning with a LOD of 21 hrs and the
 872 lunar distance was 83.4% of the present value, the Earth-Moon angular momentum at 1.4 Ga
 873 would have been approximately 95% of the present value.

874 By themselves, estimates of the past axial precession frequency from cyclostratigraphy
875 will only constrain a combination of lunar distance and LOD, and an additional independent
876 constraint is needed to determine both parameters. In particular, estimates of LOD from
877 cyclostratigraphy (e.g., as used by Mitchell & Kirscher, 2023) assume conservation of the
878 present Earth-Moon angular momentum and cannot provide a test of the hypothesis of a constant
879 LOD in the Proterozoic, because if LOD remained constant during an extended period the Earth-
880 Moon angular momentum had to increase with time.

881 **9 Conclusions**

882 We presented here two methods, TimeOptB and TimeOptBMCMC, to determine the
883 frequencies of astronomical cycles in the geologic past recorded by stratigraphic sequences. The
884 results show a decrease in the Earth's axial precession frequency from about 88.2 arcsec/year (a
885 period of 14.7 kyr) in the Mesoproterozoic (1.4 Ga) to 51.2 arcsec/year (25.3 kyr) in the Eocene
886 (55 Ma). Our results imply that at 1.4 Ga Earth days were ~18.4 hours long and that the Moon
887 was 12% closer to the Earth compared to the present (assuming that the angular momentum of
888 the Earth-Moon system was conserved).

889 Stratigraphic data invariably contain “geological noise” unrelated to astronomical
890 forcing, and resultant estimates of astronomical frequencies are inevitably uncertain. By applying
891 a Bayesian formulation, we determine posterior probability distributions that describe how much
892 each astronomical frequency can vary while fitting the observed data. We also describe a Monte
893 Carlo procedure to test whether astronomical cycles are significant over a noisy background of
894 sediment property variations.

895 A key assumption of our methods is that sedimentation rate remains constant in the
896 studied interval. This conservative requirement keeps the analysis simple and ensures that
897 recovered astronomical cycles are not the result of overfitting due to arbitrary changes in
898 sedimentation rate. We plan to investigate relaxing this assumption in future developments, for
899 example using “sedimentation templates” (Meyers, 2019) or age models defined by a number of
900 age-depth tie points (e.g., Haslett & Parnell, 2008). Variations in the age-depth relationship
901 should be kept as small as possible to avoid overfitting, and a sound significance analysis should
902 be performed to help guard against artificially identifying astronomical cycles.

903 While the constant sedimentation rate assumption restricts the range of suitable
904 cyclostratigraphic records, the examples shown here demonstrate that relatively short
905 stratigraphic intervals (spanning as little as ~600 kyr) provide valid estimates of past
906 astronomical frequencies. The methods we presented are well suited to recover from the
907 geological record the history of variation in the Earth's axial precession frequency, the
908 fundamental Solar system frequencies, and the periods of the resultant astronomical insolation
909 rhythms. The results will be useful to constrain the past history of the Earth-Moon and Solar
910 system, to inform models of past tidal dissipation, and to improve astrochronology estimates,
911 especially those based on climatic precession and obliquity cycles.

912

913 **Acknowledgments**

914 The authors declare no conflict of interest. This work was funded by the Heising-Simons
915 Foundation under grant # 2021-2798 (Malinverno) and grant # 2021-2797 (Meyers). The authors

916 thank the members of the CycloAstro project for valuable feedback throughout the development
917 of this study.

918

919 **Open Research**

920 The Xiamaling Formation Cu/Al data (Zhang et al., 2015) and Walvis Ridge a* data
921 (Zachos et al., 2004) used as examples in this study have been previously published and are also
922 accessible with the function ‘getData’ of the ‘Astrochron’ package for R (Meyers, 2014). The
923 prototype code for the TimeOptB and TimeOptBMCMC analyses presented in this work was
924 created in MATLAB and is being used and tested on additional data by CycloAstro graduate
925 students advised by the authors, whose results have not been yet published. The algorithm will
926 be made available in the ‘Astrochron’ package following publication of additional results and
927 translation into the free statistical software R.

928

929 **References**

- 930 Ajibade, R., Meyers, S. R., Lantink, M. L., Malinverno, A., Hinnov, L. A., & Carroll, A. R.
 931 (2023). Earth-Moon History and Astronomical Parameters: Constraints from the Permian
 932 and Proterozoic. Presented at the 2023 AGU Fall Meeting, Abstract PP21D-1339, San
 933 Francisco, CA.
- 934 Andersen, N. (1974). On the calculation of filter coefficients for maximum entropy spectral
 935 analysis. *Geophysics*, 39(1), 69–72. <https://doi.org/10.1190/1.1440413>
- 936 Bartlett, B. C., & Stevenson, D. J. (2016). Analysis of a Precambrian resonance-stabilized day
 937 length. *Geophys. Res. Lett.*, 43, 5716–5724, doi:10.1002/2016GL068912.
- 938 Berger, A., & Loutre, M. F. (1994). Astronomical forcing through geological time. *Spec. Publ.*
 939 *Int. Ass. Sediment.*, 19, 15–24.
- 940 Brooks, S., Gelman, A., Jones, G. L., & Meng, X.-L. (2011). *Handbook of Markov Chain Monte*
 941 *Carlo*. Boca Raton, Florida: Chapman & Hall/CRC.
- 942 Burg, J. P. (1967). Maximum entropy spectral analysis. Presented at the 37th Annual
 943 International Meeting, Society of Exploration Geophysicists, Oklahoma City, Oklahoma.
- 944 Carlin, B. P., & Louis, T. A. (2000). *Bayes and Empirical Bayes Methods for Data Analysis*.
 945 Boca Raton, Florida: Chapman and Hall/CRC.
- 946 Casella, G. (1985). An Introduction to Empirical Bayes Data Analysis. *The American*
 947 *Statistician*, 39(2), 83–87. <https://doi.org/10.2307/2682801>
- 948 Chatfield, C. (1989). *The Analysis of Time Series: An Introduction*. London: Chapman and Hall.
- 949 Cox, D. R., & Miller, H. D. (1965). *The Theory of Stochastic Processes*. London: Chapman and
 950 Hall.
- 951 Darwin, S. G. H. (1898). *The Tides and Kindred Phenomena in the Solar System: The Substance*
 952 *of Lectures Delivered in 1897 at the Lowell Institute, Boston, Massachusetts*. London:
 953 John Murray.
- 954 Dettmer, J., Molnar, S., Steininger, G., Dosso, S. E., & Cassidy, J. F. (2012). Trans-dimensional
 955 inversion of microtremor array dispersion data with hierarchical autoregressive error
 956 models. *Geophysical Journal International*, 188(2), 719–734.
 957 <https://doi.org/10.1111/j.1365-246X.2011.05302.x>
- 958 Farhat, M., Laskar, J., & Boué, G. (2022). Constraining the Earth’s Dynamical Ellipticity From
 959 Ice Age Dynamics. *Journal of Geophysical Research: Solid Earth*, 127(5),
 960 e2021JB023323. <https://doi.org/10.1029/2021JB023323>
- 961 Farhat, M., Auclair-Desrotour, P., Boué, G., & Laskar, J. (2022). The resonant tidal evolution of
 962 the Earth-Moon distance. *Astron. Astrophys.*, 665, L1. [https://doi.org/10.1051/0004-](https://doi.org/10.1051/0004-6361/202243445)
 963 [6361/202243445](https://doi.org/10.1051/0004-6361/202243445)
- 964 Fitzpatrick, R. (2012). *An Introduction to Celestial Mechanics*. Cambridge: Cambridge
 965 University Press. <https://doi.org/10.1017/CBO9781139152310>
- 966 Gelman, A. B., Carlin, J. S., Stern, H. S., & Rubin, D. B. (2004). *Bayesian Data Analysis* (2nd
 967 ed.). Boca Raton, Florida: Chapman and Hall/CRC.
- 968 Ghelichkhan, S., Fuentes, J. J., Hoggard, M. J., Richards, F. D., & Mitrovica, J. X. (2021). The
 969 precession constant and its long-term variation. *Icarus*, 358, 114172.
 970 <https://doi.org/10.1016/j.icarus.2020.114172>
- 971 Gilks, W. R., Richardson, S., & Spiegelhalter, D. J. (1996). *Markov chain Monte Carlo in*
 972 *practice*. London: Chapman and Hall.

- 973 Haario, H., Saksman, E., & Tamminen, J. (2001). An adaptive Metropolis algorithm. *Bernoulli*,
 974 7(2), 223–242.
- 975 Hacking, I. (2001). *An Introduction to Probability and Inductive Logic*. Cambridge: Cambridge
 976 University Press.
- 977 Haslett, J., & Parnell, A. (2008). A simple monotone process with application to radiocarbon-
 978 dated depth chronologies. *Journal of the Royal Statistical Society: Series C (Applied*
 979 *Statistics)*, 57(4), 399–418. <https://doi.org/10.1111/j.1467-9876.2008.00623.x>
- 980 Hays, J. D., Imbrie, J., & Shackleton, N. J. (1976). Variations in the Earth’s orbit: Pacemaker of
 981 the Ice Ages. *Science*, 194, 1121–1132.
- 982 Herbert, T. D. (1994). Reading orbital signals distorted by sedimentation: Models and examples.
 983 *Spec. Publ. Int. Ass. Sediment.*, 19, 483–507.
- 984 Hinnov, L. A. (2013). Cyclostratigraphy and its revolutionizing applications in the earth and
 985 planetary sciences. *GSA Bulletin*, 125(11–12), 1703–1734.
 986 <https://doi.org/10.1130/B30934.1>
- 987 Hoang, N. H., Mogavero, F., & Laskar, J. (2021). Chaotic diffusion of the fundamental
 988 frequencies in the Solar System. *Astronomy & Astrophysics*, 654, A156.
 989 <https://doi.org/10.1051/0004-6361/202140989>
- 990 Lantink, M. L., Davies, J. H. F. L., Ovtcharova, M., & Hilgen, F. J. (2022). Milankovitch cycles
 991 in banded iron formations constrain the Earth–Moon system 2.46 billion years ago.
 992 *Proceedings of the National Academy of Sciences*, 119(40), e2117146119.
 993 <https://doi.org/10.1073/pnas.2117146119>
- 994 Laskar, J. (2020). Chapter 4 - Astrochronology. In F. M. Gradstein, J. G. Ogg, M. D. Schmitz, &
 995 G. M. Ogg (Eds.), *Geologic Time Scale 2020* (pp. 139–158). Elsevier.
 996 <https://doi.org/10.1016/B978-0-12-824360-2.00004-8>
- 997 Laskar, J., Robutel, P., Joutel, F., Gastineau, M., Correia, A. C. M., & Levrard, B. (2004). A
 998 long-term numerical solution for the insolation quantities of the Earth. *Astron.*
 999 *Astrophys.*, 428, 261–285.
- 1000 Ma, C., Meyers, S. R., & Sageman, B. B. (2017). Theory of chaotic orbital variations confirmed
 1001 by Cretaceous geological evidence. *Nature*, 542(7642), 468–470.
 1002 <https://doi.org/10.1038/nature21402>
- 1003 Malinverno, A. (2002). Parsimonious Bayesian Markov chain Monte Carlo inversion in a
 1004 nonlinear geophysical problem. *Geophys. J. Int.*, 151, 675–688.
 1005 <https://doi.org/10.1046/j.1365-246X.2002.01847.x>
- 1006 Malinverno, A., & Briggs, V. A. (2004). Expanded uncertainty quantification in inverse
 1007 problems: Hierarchical Bayes and empirical Bayes. *Geophysics*, 69, 1005–1016.
 1008 <https://doi.org/10.1190/1.1778243>
- 1009 Mann, M. E., & Lees, J. M. (1996). Robust estimation of background noise and signal detection
 1010 in climatic time series. *Climatic Change*, 33, 409–445.
- 1011 Metropolis, N., Rosenbluth, A. W., Rosenbluth, M. N., Teller, A. H., & Teller, E. (1953).
 1012 Equation of state calculations by fast computing machines. *J. Chem. Phys.*, 21, 1087–
 1013 1092.
- 1014 Meyers, S. R. (2014). Astrochron: An R Package for Astrochronology. Retrieved from
 1015 <https://cran.r-project.org/package=astrochron>
- 1016 Meyers, S. R. (2015). The evaluation of eccentricity-related amplitude modulation and bundling
 1017 in paleoclimate data: An inverse approach for astrochronologic testing and time scale

- 1018 optimization. *Paleoceanography*, 30(12), 1625–1640.
 1019 <https://doi.org/10.1002/2015PA002850>
- 1020 Meyers, S. R. (2019). Cyclostratigraphy and the problem of astrochronologic testing. *Earth-*
 1021 *Science Reviews*, 190, 190–223. <https://doi.org/10.1016/j.earscirev.2018.11.015>
- 1022 Meyers, S. R., & Malinverno, A. (2018). Proterozoic Milankovitch cycles and the history of the
 1023 solar system. *Proc. Nat. Acad. Sci.*, 115, 6363–6368.
 1024 <https://doi.org/10.1073/pnas.1717689115>
- 1025 Meyers, S. R., & Peters, S. E. (2022). Exploring the depths of Solar System evolution.
 1026 *Proceedings of the National Academy of Sciences*, 119(43), e2216309119.
 1027 <https://doi.org/10.1073/pnas.2216309119>
- 1028 Milanković, M. (1941). *Canon of insolation and the ice-age problem: (Kanon der*
 1029 *Erdbestrahlung und seine Anwendung auf das Eiszeitenproblem) Belgrade, 1941.*
 1030 Jerusalem: Israel Program for Scientific Translations; [available from U.S. Department of
 1031 Commerce, Clearinghouse for Federal Scientific and Technical Information, Springfield,
 1032 Va.].
- 1033 Mitchell, R. N., & Kirscher, U. (2023). Mid-Proterozoic day length stalled by tidal resonance.
 1034 *Nature Geoscience*, 16(7), 567–569. <https://doi.org/10.1038/s41561-023-01202-6>
- 1035 Munk, W. H., & MacDonald, G. J. F. (1960). *The Rotation of the Earth: A Geophysical*
 1036 *Discussion*. Cambridge, UK: Cambridge University Press.
- 1037 Neal, R. N. (1993). *Probabilistic inference using Markov chain methods* (Technical Report
 1038 CRG-TR-93-1). Department of Computer Science, University of Toronto. Retrieved from
 1039 <https://www.cs.toronto.edu/~radford/ftp/review.pdf>
- 1040 Olsen, P. E., Laskar, J., Kent, D. V., Kinney, S. T., Reynolds, D. J., Sha, J., & Whiteside, J. H.
 1041 (2019). Mapping Solar System chaos with the Geological Orrery. *Proceedings of the*
 1042 *National Academy of Sciences*, 116(22), 10664–10673.
 1043 <https://doi.org/10.1073/pnas.1813901116>
- 1044 Pälike, H., Laskar, J., & Shackleton, N. J. (2004). Geologic constraints on the chaotic diffusion
 1045 of the Solar System. *Geology*, 32, 929–932. <https://doi.org/10.1130/G20750.1>
- 1046 Piana Agostinetti, N., & Malinverno, A. (2010). Receiver function inversion by trans-
 1047 dimensional Monte Carlo sampling. *Geophys. J. Int.*, 181, 858–872.
 1048 <https://doi.org/10.1111/j.1365-246X.2010.04530.x>
- 1049 Priestley, M. B. (1981). *Spectral Analysis and Time Series*. New York: Academic Press.
- 1050 Roberts, G. O., & Rosenthal, J. S. (2001). Optimal Scaling for Various Metropolis-Hastings
 1051 Algorithms. *Statistical Science*, 16(4), 351–367.
- 1052 Roberts, G. O., & Rosenthal, J. S. (2009). Examples of Adaptive MCMC. *Journal of*
 1053 *Computational and Graphical Statistics*, 18(2), 349–367.
 1054 <https://doi.org/10.1198/jcgs.2009.06134>
- 1055 Sambridge, M., & Mosegaard, K. (2002). Monte Carlo methods in geophysical inverse problems.
 1056 *Rev. Geophys.*, 40(3), 1009. <https://doi.org/10.1029/2000RG000089>
- 1057 Sen, M. K., & Stoffa, P. L. (2013). *Global Optimization Methods in Geophysical Inversion* (2nd
 1058 ed.). Cambridge, New York: Cambridge University Press.
- 1059 Sinnesael, M., De Vleeschouwer, D., Zeeden, C., Batenburg, S. J., Da Silva, A.-C., de Winter, N.
 1060 J., et al. (2019). The Cyclostratigraphy Intercomparison Project (CIP): consistency,
 1061 merits and pitfalls. *Earth-Science Reviews*, 199, 102965.
 1062 <https://doi.org/10.1016/j.earscirev.2019.102965>

- 1063 Smith, D. G. (2023). The Orbital Cycle Factory: Sixty cyclostratigraphic spectra in need of re-
1064 evaluation. *Palaeogeography, Palaeoclimatology, Palaeoecology*, 628, 111744.
1065 <https://doi.org/10.1016/j.palaeo.2023.111744>
- 1066 Ulrych, T. J., & Bishop, T. N. (1975). Maximum entropy spectral analysis and autoregressive
1067 decomposition. *Reviews of Geophysics*, 13(1), 183–200.
1068 <https://doi.org/10.1029/RG013i001p00183>
- 1069 Walker, J. C. G., & Zahnle, K. J. (1986). Lunar nodal tide and distance to the Moon during the
1070 Precambrian. *Nature*, 320, 600–602.
- 1071 Waltham, D. (2015). Milankovitch Period Uncertainties and Their Impact On Cyclostratigraphy.
1072 *Journal of Sedimentary Research*, 85(8), 990–998. <https://doi.org/10.2110/jsr.2015.66>
- 1073 Weedon, G. P. (2022). Problems with the current practice of spectral analysis in
1074 cyclostratigraphy: Avoiding false detection of regular cyclicity. *Earth-Science Reviews*,
1075 235, 104261. <https://doi.org/10.1016/j.earscirev.2022.104261>
- 1076 Wu, Y., Malinverno, A., Meyers, S. R., & Hinnov, L. A. (2023). Earth's axial precession
1077 frequency, length of day, lunar distance, and insolation periodicities over the past 650
1078 Myr from cyclostratigraphy. Presented at the 2023 AGU Fall Meeting, Abstract ID
1079 1340823, San Francisco, CA.
- 1080 Zachos, J. C., Kroon, D., Blum, P., & others. (2004). *Proc. ODP, Init. Repts.*, 208. College
1081 Station, TX: Ocean Drilling Program.
- 1082 Zahnle, K., & Walker, J. C. G. (1987). A constant daylength during the Precambrian era?
1083 *Precambrian Res.*, 37, 95–105.
- 1084 Zeebe, R. E., & Lourens, L. J. (2019). Solar System chaos and the Paleocene–Eocene boundary
1085 age constrained by geology and astronomy. *Science*, 365(6456), 926–929.
1086 <https://doi.org/10.1126/science.aax0612>
- 1087 Zeeden, C., Kaboth, S., Hilgen, F. J., & Laskar, J. (2018). Taner filter settings and automatic
1088 correlation optimisation for cyclostratigraphic studies. *Computers & Geosciences*, 119,
1089 18–28. <https://doi.org/10.1016/j.cageo.2018.06.005>
- 1090 Zhang, S., Wang, X., Hammarlund, E. U., Wang, H., Costa, M. M., Bjerrum, C. J., et al. (2015).
1091 Orbital forcing of climate 1.4 billion years ago. *Proceedings of the National Academy of*
1092 *Sciences*, 112(12), E1406–E1413. <https://doi.org/10.1073/pnas.1502239112>
- 1093 Zięba, A. (2010). Effective Number of Observations and Unbiased Estimators of Variance for
1094 Autocorrelated Data - an Overview. *Metrology and Measurement Systems*, 17(1), 3–16.
1095 <https://doi.org/10.2478/v10178-010-0001-0>
- 1096 Zięba, A., & Ramza, P. (2011). Standard Deviation of the Mean of Autocorrelated Observations
1097 Estimated with the Use of the Autocorrelation Function Estimated From the Data.
1098 *Metrology and Measurement Systems*, 18(4), 529–542. [https://doi.org/10.2478/v10178-](https://doi.org/10.2478/v10178-011-0052-x)
1099 [011-0052-x](https://doi.org/10.2478/v10178-011-0052-x)
- 1100